Carbon Dioxide Transfer Characteristics

of Hollow-Fiber, Composite Membranes

by

Tarun Shesh

A Thesis Presented in Partial Fulfillment
Of the Requirements for the Degree
Master of Science

Approved September 2018 by the
Graduate Supervisory Committee:

Bruce Rittmann, Chair
Matthew Green
Cesar Torres

ARIZONA STATE UNIVERSITY

December 2018

ABSTRACT

Carbon dioxide (CO_2) levels in the atmosphere have reached unprecedented levels due to increasing anthropogenic emissions and increasing energy demand. CO_2 capture and utilization can aid in stabilizing atmospheric CO_2 levels and producing carbon-neutral fuels. Utilizing hollow fiber membranes (HFMs) for microalgal cultivation accomplishes that via bubbleless gas-transfer, preventing CO_2 loss to the atmosphere. Various lengths and geometries of HFMs were used to deliver CO_2 to a sodium carbonate solution. A model was developed to calculate CO_2 flux, mass-transfer coefficient (K_L), and volumetric mass-transfer coefficient (K_La) based on carbonate equilibrium and the alkalinity of the solution. The model was also applied to a sparging system, whose performance was compared with that of the HFMs. Typically, HFMs are operated in closed-end mode or open-end mode. The former is characterized by a high transfer efficiency, while the latter provides the advantage of a high transfer rate. HFMs were evaluated for both modes of operation and a varying inlet CO_2 concentration to determine the effect of inert gas and water vapor accumulation on transfer rates. For pure CO_2, a closed-end module operated as efficiently as an open-end module. Closed-end modules perform significantly worse when CO_2-enriched air was supplied. This was shown by the K_La values calculated using the model. Finally, a mass-balance model was constructed for the lumen of the membranes in order to provide insight into the gas-concentration profiles inside the fiber lumen. For dilute CO_2 inlet streams, accumulation of inert gases -- nitrogen (N_2), oxygen (O_2), and water vapor (H_2O) -- significantly affected module

performance by reducing the average CO_2 partial pressure in the membrane and diminishing the amount of interfacial mass-transfer area available for CO_2 transfer.

ACKNOWLEDGMENTS

I extend my sincere gratitude and appreciation to my advisor, Dr. Bruce Rittmann, whose support along with his meticulous and scholarly guidance throughout my graduate years has enabled me to complete this thesis.

In addition, I would like to thank the members of my committee, Dr. Mathew Green and Dr. Cesar Torres, for their advice and efforts made on my behalf. My colleagues, Dr. Everett Eustance and Dr. Sean Lai, were also invaluable for answering data-related questions and for your constant support and guidance throughout this process. I enjoyed the many discussions and I am thankful for the insightful comments and advice. This research was funded by the Swette Center for Environmental Biotechnology at Arizona State University. This project provided me with exposure to many algal biofuel technologies and their real-world applications.

I am incredibly grateful for my friends Surabhi Tanwar and Mohnish Manghnani. Thank you for your feedback and support, the many insightful conversations, and for making the many long days in the office so much more enjoyable.

Last but not the least, I extend my sincere gratitude to my parents, Madhuri Shesh and Sanjay Shesh, and my uncle Vikram Kashyap, for their unconditional love, relentless support, understanding and endurance which have endorsed me the strength to overcome many difficulties and made this thesis possible.

TABLE OF CONTENTS

Page

CHAPTER Page

LIST OF TABLES

Table Page

LIST OF FIGURES

Figure Page

Figure Page

Figure Page

Figure Page

CHAPTER 1

INTRODUCTION AND SIGNIFICANCE

1.1 The Carbon Emissions Problem

A supply of secure, reliable, equitable, affordable, and sustainable energy is vital to future prosperity. Achieving all of the attributes is possibly the greatest challenge faced by humanity in the 21st century (Lewis and Nocera, 2007). In 2016, approximately 560×10^{18} J of energy was consumed globally, which is an energy-consumption rate of ~18 terawatts (TW). Fossil fuels – coal, oil, and natural gas – which contributed nearly 85% of this energy, released nearly 34 gigatons (Gt) of carbon dioxide (CO_2) to the atmosphere (BP Energy Outlook, 2018; U.S. Energy Information Adminstration, 2017).

Global energy consumption is projected to increase by at least 10 TW by 2050 due to increases in population and gross domestic product per capita, which is an indicator of economic activity (Lewis and Nocera, 2007; World Energy Council, 2017). In a model developed by the Intergovernmental Panel on Climate Change (IPCC) to predict future energy consumption, the rate of energy consumption ($\dot{E}$) can be predicted by:

$$\dot{E} = N \cdot \left(\frac{GDP}{N}\right) \cdot \left(\frac{\dot{E}}{GDP}\right) \qquad \textbf{(1.1)}$$

Equation (1.1) says that the energy consumption rate depends on the global population (N), the globally averaged gross domestic product (GDP) per capita (GDP/N), and the energy consumed per unit of GDP or the globally averaged energy intensity (Ė/GDP).

Table 1.1 provides estimations of the energy-consumption rate assuming increases in population and gross domestic product per capita, but declines in the energy intensity. The energy intensity factors in energy efficiency, resource productivity, and improvements in energy distribution and efficiency of energy use. When the energy consumed per unit of GDP decreases, it offsets increases in population and economic activity. Nonetheless, the projected energy consumption rate is 28 TW by 2050 (Lewis and Nocera, 2007), a 65% increase over today's energy-use rate of about 17 TW.

Table 1.1. World energy statistics and projections (Lewis and Nocera, 2007).

Quantity	**Definition**	**Units**	**2001**	**2050**	**2100**
N	Population	B persons	6.145	9.4	10.4
GDP	GDP	T \$ yr^{-1}	46	140	284
GDP/N	Per capita GDP	\$ $person^{-1}$ yr^{-1}	7,470	14,900	27,300
Ė/GDP	Energy intensity	W $\$^{-1}$ yr^{-1}	0.294	0.20	0.15
Ė	Energy consumption rate	TW	13.5	27.6	43.0
C/E	Carbon intensity	kgC W^{-1} yr^{-1}	0.49	0.40	0.31
Ċ	Carbon emission rate	GtC yr^{-1}	6.57	11.0	13.3
Ċ	Equivalent CO_2 emission rate	$GtCO_2$ yr^{-1}	24.1	40.3	48.8

The World Energy Council states that, in order to achieve energy sustainability, the following factors are essential: effectively managing domestic and external primary energy sources, improving the reliability of energy infrastructure, meeting current and future energy demand, evenly distributing energy supply across the population, and developing carbon-neutral and renewable energy (World Energy Council, 2017). Some of these factors will contribute to a decrease in energy intensity. Most important is deviating from fossil-fuel-based energy by developing and utilizing carbon-neutral energy sources. Achieving energy sustainability will help preserve energy security, national security, environmental security, and economic security. It also will require vast improvements in technologies employing current carbon-based fuels and, most importantly, enormous quantities of carbon-neutral fuels (Lewis and Nocera, 2007).

Fossil fuels, particularly coal, could be used to meet the increase in energy demand to 25- to 30-TW for several centuries (Lewis and Nocera, 2007). However, utilizing fossil energy at this rate is intrinsically unsustainable, because it releases new CO_2 into the atmosphere. In 1966, about 3.6 gigatons of carbon (GtC) entered the atmosphere as a result of fossil-fuel combustion (Lower, 1999). The world C emission rate was 6.6 GtC yr^{-1} in 2001, and it could rise to 11.0 GtC yr^{-1} by 2050 (Lewis and Nocera, 2007; Nakićenović and Intergovernmental Panel on Climate Change. Working III, 2000). Much of that new C in CO_2 accumulates in the atmosphere, since the rate of removal of CO_2 through natural processes cannot match the rate of anthropogenic production.

The CO_2 concentration in the atmosphere was about 280 ppm before the start of the Industrial Revolution. The CO_2 concentration in the atmosphere is now in excess of 400 ppm, due mainly to fossil-fuel combustion, and these concentrations continue to increase. Experts on global climate predict that a CO_2 concentration greater than about 450 ppm, likely to occur by mid-century, will induce a range of disruptive effects: (i) a rise in sea levels; (ii) accelerated glacial melting; (iii) climactic disturbances affecting the amount and distribution of precipitation; (iv) hindrances to food production; (v) accelerated species extinction; (vi) positive feedback resulting from the loss of permafrost that releases CO_2 and accelerates warming and all other global impacts (Keith, 2009; Lewis and Nocera, 2007).

About one-half of the CO_2 released into the atmosphere remains there; the remainder partitions between the hydrosphere and the biosphere (Lewis and Nocera, 2007; Lower, 1999). Atmospheric CO_2 can be removed naturally through uptake by land and ocean sinks. The amount of atmospheric CO_2 has been slowly increasing over time (>2 ppm yr^{-1}) relative to the amount taken up by natural processes, due mainly to anthropogenic emissions and, to a smaller extent, land clearing (Raupach et al., 2007). It is estimated that natural processes removed roughly 12 Gt of CO_2 which is less than half of the 29 Gt emitted in 2006 (Bilanovic et al., 2009; U.S. Energy Information Administration, 2005). Oceans contain about 60 times the inorganic carbon (C_i) contained in the atmosphere due to the transformation of absorbed oceanic CO_2 into bicarbonates and carbonates in an aqueous medium. Given that the equilibration time between atmospheric CO_2 and the topmost (100 m) layer of oceans is 10 to 30 years, and

that efficient transfer occurs only in this layer, only about 10% of CO_2 added to the atmosphere is taken up by the oceans. The topmost layer of the oceans contains only about one atmosphere equivalent of CO_2; given the cumulative nature of CO_2 in the atmosphere, the uptake of this CO_2 will occur over a couple of millennia (Lewis and Nocera, 2007; Lower, 1999).

To mitigate climate risks posed by accumulating atmospheric CO_2, natural CO_2-removal processes cannot be solely relied upon, and large-scale deployment of carbon-free power is required (Solomon et al., 2009). Stabilizing CO_2 levels in the atmosphere depends on reductions in energy intensity and carbon intensity (Pielke et al., 2008). Decarbonization of the global energy system based on modestly stringent interventions could stabilize atmospheric CO_2 levels in the 550- to 650-ppm range (Lewis and Nocera, 2007; Pielke et al., 2008). The amount of such power required is similar to the current energy demand (>10 TW).

One way to reduce carbon intensity is carbon capture, sequestration, and utilization (Wang et al., 2011a). Capture of CO_2 from the flue gases of power plants is the most recognized strategy (Keith, 2009). CO_2 also can be captured from ambient air. The main technologies for CO_2 capture and sequestration from atmospheric air include: (i) chemical-reaction based schemes such as using chemical absorbents like solid amine-based resins, metal oxides like lime (CaO), or liquid absorbents like monoethanolamine (MEA); (ii) geological sequestration which involves injection of CO_2 into geological formations, the soil, deep ocean storages, saline aquifers, coupled with mineral

carbonation of CO_2; (iii) bio-fixation which involves uptake of CO_2 during photosynthesis performed by plants and microorganisms (Kumar et al., 2010; Lackner, 2003; Sadeghizadeh et al., 2017; Tebbani et al., 2014; Wang et al., 2008; Wang et al., 2011b).

Chemical-based methodologies consist of three steps: capture, transportation, and storage (Bhola et al., 2014). Using chemical methods to capture CO_2 from ambient air is expensive and energy-intensive due to the low concentration of CO_2 present in air (400 ppm); however, using highly selective sorbents have had some success in capturing CO_2 from dilute streams (Wang et al., 2011b). To aid in transportation, captured CO_2 must be converted into a supercritical fluid. Thus, transportation costs are estimated to cost about \$1 – 3 per ton per 100 km in addition to the cost of CO_2 separation and compression for transport (Wang et al., 2008). Finally, sequestration of CO_2 requires large amounts of space, and it is prone to leakage over time, which would require recapture programs in the future.

Instead of relying solely on storage of captured CO_2, utilization of captured CO_2 is a viable option. CO_2 can be used in the manufacture of paper products, paint, plastic, solvents, and more. (Bhola et al., 2014). However, these industries consume only minute amounts of CO_2. Bio-fixation of captured CO_2 is relatively efficient, economically feasible and sustainable in the long-term. Bio-fixation can be carried out by terrestrial plants and photosynthetic microorganisms (Kumar et al., 2010; Tebbani et al., 2014). Since most capture methods require concentrated streams of CO_2, utilizing CO_2 captured

from the flue gas of power plants, and maybe air, on-site could be an economically viable mitigation technique.

Today, a multitude of strategies will be needed to slow and eventually reverse the buildup of CO_2 in the atmosphere: increased energy efficiency (i.e., decreasing energy use per unit of product, process or service); increased use of renewable energy (i.e., carbon-neutral energy resources, such as wind and solar photovoltaics); and capture and sequestration of CO_2 emitted during the combustion of fossil energy. A fourth strategy is to capture CO_2 and use it to produce energy and products that otherwise would have come from fossil sources. This thesis deals directly with this fourth strategy: making good use of captured CO_2.

1.2 Benefits of Microalgae

Biofuels are among the alternatives to fossil energy. The basic principle of biofuel is that sunlight drives photosynthesis, which fixes the C in CO_2 into organic matter that can be used as fuel feedstock that replaces fossil sources. Because the energy comes from the sun and the CO_2 is fixed contemporaneously with the biofuels use, the biofuel can be renewable and carbon-neutral.

First-generation biofuels were derived from terrestrial crops such as sugarcane, sugar beet, and maize. Commercial biodiesel is commonly produced from canola oil, animal fat, palm oil, corn oil, waste cooking oil, and jatropha oil (Barnwal and Sharma, 2005; Kulkarni and Dalai, 2006). They place an enormous strain on world food markets,

contribute to water shortages, increase the use of fertilizers, and accelerate the destruction of biodiversity. Therefore, first-generation biofuels are not sustainable alternatives to fossil fuels (Crutzen et al., 2008).

Second-generation biofuels are derived from lignocellulosic agriculture and forest residues, i.e., from the whole plant matter of dedicated energy crops feedstocks address some of the above problems (Kendall and Chang, 2009; Moore, 2008). Lignocellulose is widely available, since it makes up majority of the non-edible materials from plants (Naik et al., 2010). Sources include agricultural residues, wood processing waste – leaves, straw or wood chips – and non-edible parts of sugarcane (Kendall and Chang, 2009; Moore, 2008). Lignocellulose serves as feedstock for bioethanol production (Schenk et al., 2008). Lignocellulosic plant biomass also can be burned to produce heat and electricity or can yield liquid biofuels. Additionally, production of second-generation biofuels leads to the consumption of waste residues, usage of non-arable land, promoting rural development, and improving economic conditions in emerging and developing regions (Sims et al., 2010).

For first- and second-generation biofuels, only a small fraction of humans' energy demand can be satisfied despite the apparent abundance of plant biomass. Furthermore, commercialization of second-generation biofuels is hindered by: (i) transport costs of biomass to biorefineries; (ii) expensive pre-treatment processes to expose the cellulose and hemicellulose for hydrolysis; (iii) differences in characteristics of various feedstocks for multi-feedstock plants; and (iv) stability of lignin in woody biomass, making it

difficult for extraction and biochemical conversion (Brennan and Owende, 2010; Sims et al., 2010).

Even though they cannot come close to meeting the demand for energy feedstock, the first two generations of biofuels put added pressure on land use and water resources.

Third-generation biofuels, derived from microalgae, are alternative energy resources devoid of the major drawbacks associated with first- and second-generation biofuels (Xu et al., 2006). Microalgae accumulate lipids and have biomass areal productivity as much as 50 times higher than that of switchgrass, which is one of the fastest growing crops used for bioenergy production. Additionally, microalgae can trap up to 9% of solar energy compared to switchgrass, which traps $\leq 0.5\%$ of solar energy (Chisti, 2008; Lewis and Nocera, 2007; Li et al., 2008). In addition to high areal productivity, microalgae offer the following advantages for biofuel production: less water consumed than terrestrial crops and tolerance to high CO_2 content in gas streams. The high productivity of microalgae and the possibility for them to utilize concentrated sources of CO_2 make them an especially attractive means to make good use of captured CO_2 (Chisti, 2008; Lewis and Nocera, 2007). Furthermore, microalgae are capable of producing high-value products, such as natural pigments, high-quality proteins, beta-carotene, and eicosapentaenoic acid, which are economically important in order to commercialize algal biomass on a large-scale (Carvalho and Malcata, 2000; Klausner, 1986; Terry and Raymond, 1985).

Despite microalgae's inherent potential as a biofuel resource, many challenges have impeded the development of algal biofuel technology to commercial-scale: (i) water evaporation and CO_2 losses to the atmosphere for commonly used open ponds; (ii) difficulty maintaining culture stability due to susceptibility to microbial contamination; (iii) the potential for negative energy balance after accounting for requirements in water pumping, CO_2 transfer, harvesting, and extraction, the last two being significant expenses; and (iv) poor efficacy of supplying CO_2 and nutrients, which dictates lipid productivity (Carvalho and Malcata, 2001; Ferreira et al., 1998; Ono and Cuello, 2006; Quinn and Davis, 2015; Ugwu et al., 2008; Wijffels and Barbosa, 2010).

1.3 Relationships Between CO_2 and Microalgae

Biofuel production from photoautotrophic algae is a promising strategy for controlling CO_2 released by combustion, for example, from power plants doing fossil fuel combustion (Kim et al., 2011; Sawayama et al., 1995; Yun et al., 1997). Microalgae can utilize CO_2 from the atmosphere and can fix CO_2 from soluble carbonates – sodium bicarbonate, $NaHCO_3$, and sodium carbonate, Na_2CO_3 (Lackner, 2009; Wang et al., 2008). Microalgal biomass contains approximately 50% C by dry weight, and the carbon is typically derived from CO_2, which is fixed during photosynthesis (Kim et al., 2011; Miron et al., 2003). Producing 100 dry tons of algal biomass fixes roughly 50 tons of C, or 183 tons of CO_2.

Chlorella is one of the faster growing microalgae, and it is capable of producing microalgal oil at a rate equivalent to 3,200 GJ ha^{-1} per year. This rate is sufficient to replace 300 EJ per year (9.5 TW) of energy supplied by fossil fuels by 2050, thus mitigating about 6.5 GtC per year using only a small proportion of excess arable land available (Wang et al., 2008).

An adequate CO_2 supply is required for optimal growth conditions for microalgae. CO_2 must be continually fed during the daylight hours to supply the C for synthesis, and CO_2 delivery can also be used to control the pH (Nguyen and Rittmann, 2016).

The rate of CO_2 delivery depends on the CO_2 concentration in the supplied gas. Mass transfer is limited when atmospheric air is used, since the concentration of CO_2 is very low for cultivation (400 ppm), resulting in low CO_2 transfer rates from the air to the culture (Putt et al., 2011; Wang et al., 2008). Increasing the CO_2 concentration in the gas's influent stream can increase CO_2 transfer into the culture medium, as shown in Figure 1.1: higher CO_2 concentrations in the gas's influent stream corresponds to higher dissolved inorganic carbon (DIC) concentrations in the culture medium, which allow for higher algal growth rates (Eustance et al., 2016).

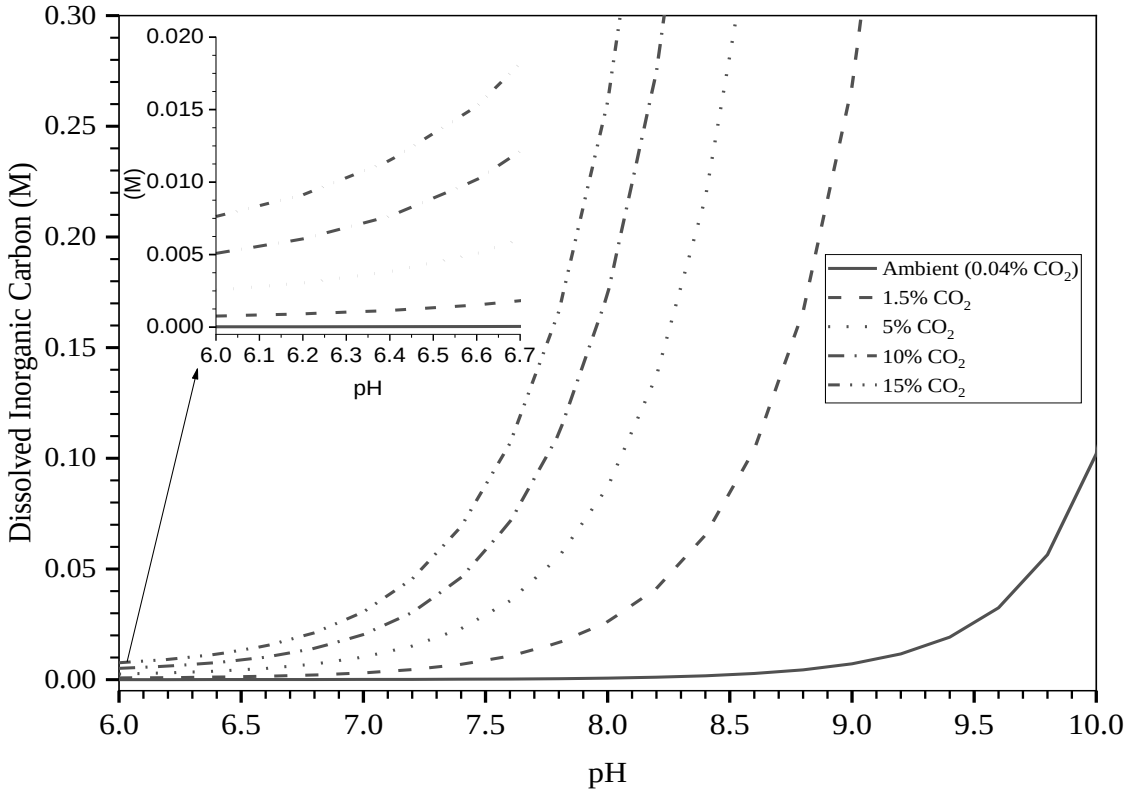

Figure 1.1. Effects of pH and CO_2 in gaseous phase on total DIC.

DIC exists as several interconvertible chemical forms based on the pH of the solution: dissolved CO_2 ($CO_{2(aq)}$), carbonic acid (H_2CO_3), bicarbonate (HCO_3^-), and carbonate (CO_3^{2-}), as shown in Figure 1.2 (Putt et al., 2011; Stumm and Morgan, 1996). CO_2 dissolves in water to form $CO_{2(aq)}$, which is converted to H_2CO_3. The concentration of H_2CO_3 is combined with that of $CO_{2(aq)}$ and termed $H_2CO_3^*$. Optimal microalgal growth typically occurs in the pH range of 8 – 10 (Putt et al., 2011; Wang et al., 2008), and the concentration of $H_2CO_3^*$ is very low, with HCO_3^- comprising most of the DIC. When the pH exceeds 10.3, CO_3^{2-} dominates the DIC, and this can lead to the precipitation of solids such as $CaCO_3$, which lowers the DIC concentration and also the

pH. When the pH drops below 8, dissolved CO_2 may be lost by volatilization, which lowers the DIC available for algal uptake, but increases the pH (Eustance et al., 2016; Putt et al., 2011). Thus, this thesis focuses on measurements for a pH range of 8 – 10, since it is ideal for microalgae growth and avoids DIC losses by volatilization or precipitation.

Several important species of cyanobacteria and algae – e.g., *Synechocystis* sp. PCC6803 and *Chlorella sorokiniana* – take up C_i only as $CO_{2(aq)}$ and HCO_3^- (Kim et al., 2011; Nielsen and Jensen, 1958). Microalgae and cyanobacteria have developed a series of C_i transporters or enzymes called carbon anhydrases to enable the accumulation of intracellular HCO_3^- 1000 times higher than the HCO_3^- concentration in the growth medium (Eustance et al., 2016; Nguyen and Rittmann, 2016). This is known as the CO_2-concentrating mechanism (CCM). Five C_i transporters work in tandem in CCM: three for HCO_3^- and two for dissolved CO_2. The growth medium's C_i concentration and pH, which controls C_i speciation, affect which transporter is dominant (Nguyen and Rittmann, 2016). Higher pH due to photosynthesis and inadequate C_i supply can lead to CO_3^{2-} being the dominant C_i species, which cannot be utilized by the CCM C_i transporters (Nguyen and Rittmann, 2016; Price, 2011).

Because pH and C_i speciation in the liquid medium affect how C_i is available for growth, precise control over CO_2 delivery and pH are required. For example, if pure CO_2 is delivered to the liquid phase without control, the pH could drop too low to support optimal growth of the culture.

The culture medium's alkalinity and pH are affected by C_i uptake during photosynthesis (Goldman et al., 1982). Alkalinity also can change depending on the source of nitrogen used in the medium. Alkalinity and DIC increase if NO_3^- is used as the N source, but alkalinity and DIC decrease if NH_4^+ is used as the N source (Nguyen and Rittmann, 2015). Alkalinity and DIC can be held constant if ammonium and nitrate are both used equally as N sources (Nguyen and Rittmann, 2015). Since pH, C_i, and alkalinity are linked, changes in alkalinity can complicate pH and C_i control. A solution to controlling the pH is through using a pH-stat to automatically add CO_2 gas to the growth medium, in addition to utilizing NH_4NO_3 as the N source to stabilize the alkalinity of the growth medium (Nguyen and Rittmann, 2016).

Apart from pH, CO_2 solubility also depends on the temperature of the medium and the influent gas's CO_2 partial pressure. Determining CO_2 solubility in the growth medium is crucial since this will establish the amount of DIC available for biomass synthesis. CO_2 solubility decreases as the temperature of the medium increases. However, increasing the partial pressure of CO_2 increases solubility according to Henry's law, which states that the partial pressure of a gas is directly proportional to its equilibrium concentration in solution. Thus, increasing the partial pressure of CO_2 increases the DIC in the medium, as shown in Figure 1.1 (Bhola et al., 2014; Lower, 1999). CO_2 solubility can also be increased by lowering the temperature of the growth medium (Bhola et al., 2014).

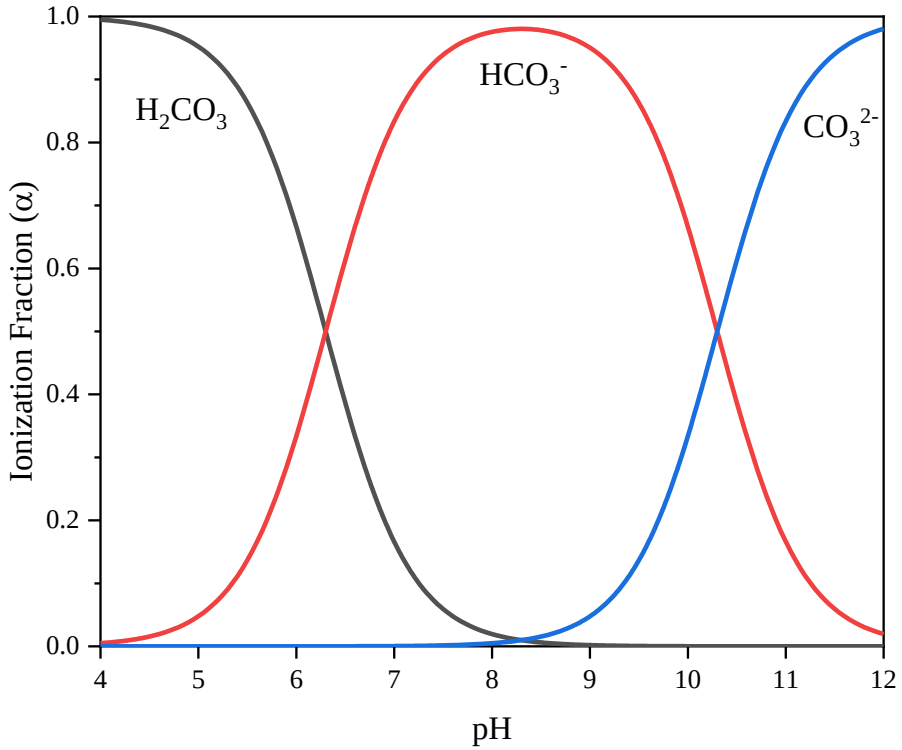

Figure 1.2. DIC speciation based on pH and for a fixed C_i.

1.4 Sources of Concentrated CO_2

Common sources of concentrated CO_2 streams include flue gas, off-gas of anaerobic fermentation, and purchased CO_2 (Yen et al., 2015; Zhu, 2015). Industrial exhaust gases – flue gas and flaring gas – contain as much as 15% (v/v) CO_2, providing a CO_2-rich source for microalgal growth (Wang et al., 2008). Co-location of microalgae cultivation systems adjacent to point sources of CO_2 emission could be advantageous,

since the CO_2 released at night can be stored for uptake during the day, thus eliminating transportation and CO_2 compression costs (Putt et al., 2011; Wang et al., 2008).

Table 1.2 shows the biomass productivities (P) and CO_2 fixation rates of (P_{CO_2}) of selected microalgal species for different CO_2 input streams. The information suggests that *S. obliquus* and *C. kessleri* have a higher productivity and higher CO_2 fixation rate as the concentration of the supplied CO_2 increases, which means that some microalgal species can tolerate higher CO_2 concentrations. This is important, since flue gas can be delivered directly to algal cultures without inhibiting growth in those cases (Yun et al., 1997).

Table 1.2. CO_2 fixation rates of some microalgal strains. Adapted from (Wang et al., 2008).

Microalga	**CO_2 %**	**T°C**	**P g L^{-1} per day**	**P_{CO_2} g L^{-1} per day**	**Notes**
Chlorella kessleri	18	30	0.087	0.163	
Chlorella vulgaris	Air	25	0.040	0.075	Watanabe's medium
Chlorella vulgaris	Air	25	0.024	0.045	Low-N medium
Scenedesmus obliquus	Air	--	0.009	0.016	Wastewater, outdoor, winter
Scenedesmus obliquus	Air	--	0.016	0.031	Wastewater, outdoor, summer
Scenedesmus obliquus	18	30	0.14	0.26	

Apart from CO_2, flue gas also contains N_2, O_2, and NO_x, and it may also contain SO_2 and heavy metals such as nickel, vanadium, and mercury (Bhola et al., 2014; Kumar et al., 2010; Wang et al., 2008). Nitrogen monoxide (NO) can be toxic to many algal species (Tebbani et al., 2014). Sulfur dioxide also can acidify the culture medium due to its conversion to sulfurous acid (H_2SO_3) (Bhola et al., 2014; Eustance et al., 2016; Tebbani et al., 2014). Heavy metals can reduce growth by inhibiting enzyme activity (Kumar et al., 2010).

Microalgae are typically cultivated in either open ponds or photobioreactors (PBR). Open ponds are characterized by a moderate ratio of the illuminated surface area to culture volume ($3 – 10\ m^{-1}$), while PBRs can have higher surface-area-to-volume ratios ($25 – 125\ m^{-1}$) (Wang et al., 2008). However, PBRs provide better control of operating conditions, minimize contamination, and achieve higher biomass density, biomass productivity, and CO_2-fixation rates (Sadeghizadeh et al., 2017; Wang et al., 2008). PBRs require a higher capital investment compared to open ponds, higher operating costs also can lead to poorer cost effectiveness (Kumar et al., 2010).

The cost of supplying CO_2 to large-scale algal cultures could be the determining factor on whether the process is profitable (Manganaro et al., 2015; Tapie and Bernard, 1988). The price of CO_2 delivery is location-specific. In a comparison of two separate industrial processes, a huge cost difference was observed between an operation for beta-carotene production and another operation for algal lipid production due to the latter's adjacency to a power plant. This enabled the use of flue gas for CO_2 delivery, thus

reducing the cost of CO_2 from $150,000 per year to $50,000 per year (Sun et al., 2011). Given the high cost of CO_2 as a raw material, a high gas-transfer efficiency into the liquid phase is required to prevent wasting CO_2 by off-gassing it (Bhola et al., 2014; Ferreira et al., 1998).

The cost of CO_2 can be reduced if a source of CO_2 is available nearby, thus reducing the cost of CO_2 processing and transportation, for example, CO_2 concentrated out of flue gas from a nearby power plant (Davis et al., 2011). The cost of CO_2 extraction from flue gas using MEA is 40% cheaper than direct utilization of flue gas due to the cost of CO_2 compression associated with the latter process (Kadam, 1997; Zheng et al., 2016). The drawback of using chemical absorption processes for CO_2 capture from CO_2-laden streams using solvents – MEA, triethanolamine (TEA) and potassium carbonate – is the energy and cost associated with solvent regeneration and CO_2 recovery (Kim et al., 2013; Rahaman et al., 2011; Zheng et al., 2016).

Adding alkanolamine CO_2 absorbents – MEA, 2-amino-2-methyl-1-propanol (AMP), diethanolamine (DEA) and TEA – to the culture medium can increase the DIC available for algal uptake; however, the toxicity of such absorbents could inhibit algal growth (Kim et al., 2013). Zheng et al. proposed that a potassium carbonate solution could be used to absorb CO_2 from flue gas and then supplied to microalgae using hollow-fiber membranes. The disadvantage of this method is that at low CO_2 concentrations in the solvent, the culture could be carbon-limited resulting in microalgal growth inhibition. Additionally, the CO_2 concentration in the flue gas used could affect the energy

associated with solvent recirculation in order to maintain a high CO_2 loading to prevent carbon limitation in the culture medium.

The quality of the interface between the gaseous CO_2 phase and the liquid growth medium phase is very important, since the interface is the main limitation in utilizing gaseous nutrients (Carvalho and Malcata, 2001; Eustance et al., 2016). A high driving force in terms of a concentration gradient is desirable. Supplying air inherently leads to low CO_2 transfer rates, since air contains only about 400 ppm of CO_2 (Becker, 1994; Carvalho and Malcata, 2001). CO_2-enriched air can be utilized to provide a larger driving force; the key factors are maximizing the contact time of the CO_2 with the liquid phase before off-gassing or to increase the interfacial area per unit volume of the mass-transfer device.

Stabilizing CO_2 levels in the atmosphere will require more than simply capturing CO_2 from concentrated sources such as power plants. Capturing CO_2 emitted to the atmosphere from small and distributed sources, referred to as direct air capture (DAC), could achieve this as we transition to non-carbonaceous fuels (Lackner et al., 2001). CO_2 can be captured using either liquid solvents, solid sorbents, or via cryogenic separation (Lackner et al., 2001; Lackner, 2009; Rahaman et al., 2011). Cryogenic separation has the highest capture efficiency, but is also the most expensive DAC process and is economical only with high CO_2-bearing input streams (Rahaman et al., 2011). While solid sorbents such as the X-type zeolite, exhibit excellent performance for DAC, the heat energy required for sorbent regeneration is high in addition to the challenge of sealing the

entire structure from ambient air during the recycling step (Keith et al., 2018; Rahaman et al., 2011). Aqueous sorbents – MEA, potassium hydroxide (KOH), or sodium hydroxide (NaOH) – offer the advantages of continuous operation and longer lifetimes (Keith et al., 2018; Rahaman et al., 2011).

The amount of energy required for DAC can be mitigated by utilizing a moisture-swing cycle involving an ion exchange resin that absorbs CO_2 when dry and desorbs CO_2 when wet (Wang et al., 2011b). Recently, Carbon Engineering (CE) has developed a 1 Mt-CO_2 yr^{-1} DAC plant which uses two chemical loops: first, aqueous KOH is used as a sorbent to produce potassium carbonate (K_2CO_3), and second, calcium carbonate ($CaCO_3$) is produced by a precipitation reaction between CO_3^{2-} and Ca^{2+}. $CaCO_3$ can then be heated to produce CO_2 and CaO. CO_2 can be processed and used as a carbon source for microalgal cultivation, and the CaO can be hydrated to form $Ca(OH)_2$, the dissolution of which produces Ca^{2+} (Keith et al., 2018). CE has stated that the cost of CO_2 capture using this method could be as low as $94 per metric ton of CO_2, which is a significant decrease from a value of $600 per metric ton of CO_2 as reported by the American Physical Society in 2011 (American Physical Society, 2011; Keith et al., 2018).

1.5 Utilizing Hollow-Fiber Membranes (HFMs) for CO_2 Delivery

Carbon sequestration is a very important factor in techno-economic assessments for large-scale production of photoautotrophic algae (Sun et al., 2011). The cost of CO_2

can vary from $40 per metric ton for CO_2 from flue gas to $94 – 232 per metric ton for DAC (Davis et al., 2011; Keith et al., 2018). Thus, any captured CO_2 must be delivered efficiently for algal uptake to prevent CO_2 loss to the environment, which is undesirable since carbon capture is energy- and cost-intensive (Lackner, 2013). Producing carbon-neutral fuels requires that no CO_2 is lost to the atmosphere.

The various methods of gas-transfer include: mechanical systems to blow CO_2 into the culture (propellers and blades); bubble diffusers (perforated piping, slotted tubes, porous stones, and discs); jet aerators; carbonation columns; and hollow-fiber gas-transfer membranes (Ahmed et al., 2004; Carvalho and Malcata, 2001; Fan et al., 2007; Kumar et al., 2010).

Active modes of gas transfer involve bubbling CO_2 into the culture medium. The most commonly used approach of CO_2 delivery is sparging CO_2-enriched air into the medium through sintered porous stones placed at the bottom of the system (Kumar et al., 2010). This is a very inefficient method of gas transfer since ~ 65% of CO_2 is not transferred to the culture medium, but is lost to the atmosphere (Putt et al., 2011). The off-gassing phenomenon can be observed in Figure 1.3 (a). The concentration of influent CO_2 can be increased in order to improve transfer rates; however, an increase in CO_2 partial pressure does not mean that the CO_2 utilization efficiency will increase (Eustance et al., 2016). Often, a sump with a baffle is used in raceway ponds in order to increase CO_2 transfer efficiency to 95% (Campbell et al., 2009). However, modifications would have to be made to the existing structure of ponds to accommodate a sump.

Increasing the interfacial area available for gas-transfer and the gas-liquid contact time leads to enhanced CO_2 mass-transfer efficiencies. Due to the counter-current flow of CO_2 and liquid, carbonation columns enhance gas-liquid contact time, and they can achieve mass-transfer efficiencies as high as 83% by utilizing CO_2 concentrations of up to 90% (v/v) compared to an efficiency of ~ 35% for a sparging system (Putt et al., 2011). Achieving 100% mass-transfer efficiency without any off-gassing is not economically feasible using carbonation columns, since the CO_2 concentration in the bubble decreases exponentially as it rises through the culture medium. The height of the column required to reduce CO_2 concentration from 100% to 10% would be the same as the additional height required to reduce the concentration from 10% CO_2 to 1% CO_2 (Putt et al., 2011). An increase in the bubble size results in smaller interfacial areas available for gas-transfer lowering the mass-transfer efficiency. For large-scale cultivation systems, coalescence of bubbles in a carbonation column also leads to lower mass-transfer efficiencies (Putt et al., 2011). Sufficient mixing is required in the culture to ensure that the increased CO_2 in the liquid phase in a carbonation column is rapidly distributed to the entire culture rather than lost to the atmosphere (Eustance et al., 2016).

The CO_2-delivery rate controls the pH, available DIC, and C_i speciation in the culture medium. If the rate of CO_2 addition is greater than the CO_2 utilization rate, CO_2 will be lost to the atmosphere. This problem can be solved by a pH-controlled CO_2 delivery mechanism. Large-scale cultivation systems have massive C_i requirements, and delivery must be accomplished efficiently. The interfacial area where CO_2 comes in contact with the culture medium can be increased by diffusing CO_2 through membranes

(Lee and Hing, 1989). Since this is a bubbleless, diffusion-driven mechanism of gas-transfer, as can be seen in Figure 1.3 (b), the amount of CO_2 lost to the atmosphere is minimal, resulting in high transfer efficiencies (Putt et al., 2011). This contrasts with the sparging system shown in Figure 1.3 (a), where CO_2 gas is lost to the atmosphere as bubbles, resulting in relatively low transfer efficiencies.

Proper membrane selection is vital to reduce the resistances faced by gas transfer. For example, a membrane with a thick wall will increase the resistance faced by the diffusion of gas into the liquid face, subsequently negatively affecting transfer rates (Carvalho and Malcata, 2001). Membrane cost becomes an important factor considering that large membranes are needed, since the transfer rate is directly proportional to the interfacial area. High internal pressures need to be used to achieve economical transfer rates.

(a)

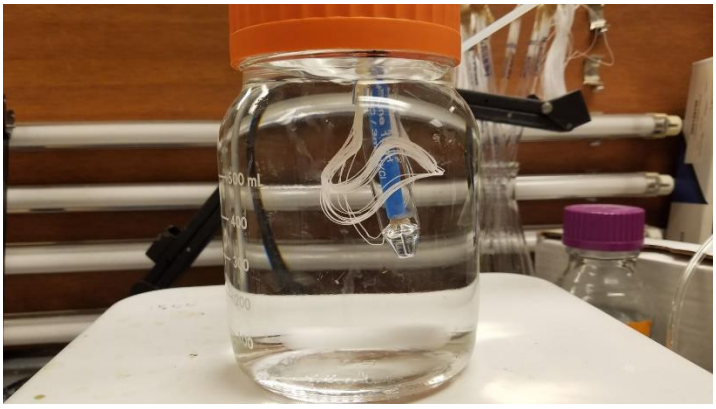

(b)

Figure 1.3. Comparison of CO_2 delivery using (a) porous stone with (b) hollow-fiber membrane (HFM).

Highly permeable silicone rubber membranes have been used in the past in order to reduce CO_2 losses to the atmosphere and precisely control CO_2 transfer rates (Lee and Hing, 1989). However, silicon membranes are quite expensive and have a thick wall.

In order to enlarge the contact area between the gaseous and liquid phase, microporous membranes can be used since the ratio of the interfacial area to volume is very high (Carvalho and Malcata, 2001). Microporous polypropylene (PP) fibers have been used in the past extensively to better understand gas transfer characteristics. However, if PP fibers are operated under high pressures, bubble formation occurs, which results in CO_2 loss to the atmosphere. This would mean that the liquid phase would also have to be pressurized to reduce the transmembrane pressure at higher operating pressures. This is a result of the porosity of these membranes (Ahmed and Semmens, 1992a; Ahmed and Semmens, 1992b). Since PP has a low bubble point, a nonporous layer can be added to reduce the porosity of the membrane and bubble formation. Polydimethylsiloxane (PDMS) coated PP fibers could handle internal gas pressures of up to 60 psi without bubble formation (Voss et al., 1999). However, PDMS coated fibers are expensive.

Mitsubishi-Rayon Co. (Japan) manufactures composite hollow-fiber membranes (HFM) that have a nonporous polyurethane core (1 μm thick) surrounded by two macroporous polyethylene layers as can be seen in Figure 1.4 (a). Figure 1.4 (b) shows the top view of a bundle of closely-packed hollow fibers. Similar to the PDMS coated membranes, the dense polyurethane core allows for higher operating pressures without

bubble formation. The increased thickness of the nonporous core increases the membrane resistance to gas-transfer; however, the ability to operate at higher pressures offsets the cost of an increased membrane resistance (Ahmed and Semmens, 1992a; Ahmed and Semmens, 1992b). These composite membranes are practical and commercially available. Using bubbleless gas-transfer of CO_2, called membrane carbonation (MC), allows precise control of the CO_2-delivery rate and minimal loss of CO_2 to the atmosphere (Kim et al., 2011).

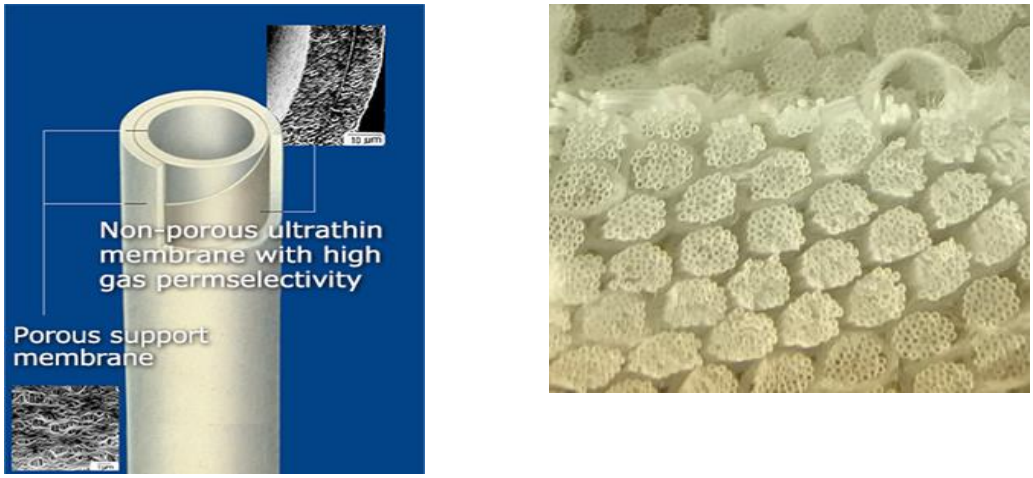

(a) (b)

Figure 1.4. Structure of a composite Mitsubishi-Rayon HFM.

The concentration of gaseous CO_2 in the membrane lumen, the concentration of dissolved CO_2 in the liquid, and the hydrodynamic conditions of the culture play important roles in the CO_2 transfer rate. Changing the CO_2 partial pressure inside the fiber can change the rate of gas-transfer, permitting accurate control over CO_2 delivery capacity (Kim et al., 2011; Kumar et al., 2010).

Typically, gas is delivered to a HFM from one end of the fiber. An important distinction is how the other end of the fiber is managed. HFMs for microalgal cultivation can be operated as open-end, closed-end, or partially open-end. The implications of each choice are profound in terms of CO_2-transfer efficiency and rate.

In a closed-end HFM, all the CO_2 supplied to the membrane diffuses across the membrane's wall into the liquid phase. Since no CO_2 exits from the far end, closed-end operation allows for 100% CO_2 transfer efficiency (Perez-Calleja et al., 2017). However, when the inlet gas is not pure CO_2, the CO_2 partial pressure in the lumen decreases along the fiber length due to the selective retention of inert gases (e.g., N_2 and O_2 in flue gas) (Ahmed et al., 2004; Ahmed and Semmens, 1992b; Ahmed and Semmens, 1992a; Perez-Calleja et al., 2017). In addition, inert gases may diffuse into the lumen; water vapor is a good example. The buildup of inert gases affects CO_2 transfer rates, since the distal end of the fiber lumen could be devoid of CO_2, thus reducing the average CO_2 partial pressure along the fiber length (Perez-Calleja et al., 2017). Back-diffusion of water vapor also poses a concern about its condensation inside the lumen, which can affect the performance of the fibers (Ahmed and Semmens, 1992a).

In an open-end HFM, gas continually flows through the membrane, which prevents or minimizes the buildup of any inert gases, which are swept out from the open end of the lumen. Thus, the CO_2-concentration is nearly uniform along the fiber length, which means that the average CO_2 concentration does not decline due to the buildup of inert gases. If the gas velocity through the membrane is high enough, the total gas

pressure can decline due to friction losses, and this will lower the partial pressure of CO_2 proportionally. The big disadvantage of an open-end HFM is that the CO_2 transfer efficiency is far smaller than 100%, because so much CO_2 is vented out the distal end (Ahmed and Semmens, 1992b; Perez-Calleja et al., 2017).

A compromise that can avoid the disadvantages of using closed-end and open-end operation is partially open-end HFM, in which only a small flow of the lumen gas is vented from the distal end. The venting rate should be set at the minimum value that precludes a significant buildup of inert gases in the lumen. The result of a good operation in the partially open-end mode is a higher transfer efficiency together with a higher transfer rate.

1.6 Objectives

The first objective of my work is to quantify the impacts of influent CO_2 concentration on the rate of CO_2 delivery using bubbleless HFMs. The partial pressure of CO_2 supplied determines the maximum concentration gradient, which is the driving force for CO_2 transfer across the membrane. In the liquid phase, the pH and DIC concentration affect the actual concentration gradient, since they control $CO_{2(aq)}$. The accumulation of inert gases such as nitrogen (N_2) and oxygen (O_2) when using input CO_2 less than 100%, along with the back-diffusion of water vapor, can adversely affect the CO_2 flux.

A second objective is to quantify the efficiency of CO_2 transfer with the bubbleless HFMs. Therefore, I conducted mass balances to determine the amount of CO_2

lost under various operating conditions such as, varying inlet CO_2 composition, and varying the restriction on the effluent flow from the membrane lumen from completely open to the atmosphere to completely closed.

I also developed a mathematical model to evaluate the partial pressures of CO_2, N_2, O_2, and water vapor within the membrane lumen to determine the length of the fibers involved in mass transport.

My thesis is organized in the following chapters to achieve the goals outlined:

1. In Chapter 2, I highlight the materials and methodologies I used to conduct the mass-transfer and mass-balance experiments.
2. In Chapter 3, I discuss the model I developed to calculate the mass transfer coefficient and flux of CO_2 across the membrane based on pH.
3. In Chapter 4, I provide the theoretical background behind the model I developed to evaluate partial pressures inside the membrane lumen. I use the model to evaluate varying compositions of inlet CO_2 and the effect of a closed, open, or partially-open system on the gas profile inside the membrane lumen. The transfer efficiency and transfer rate of the various modes of operation also are discussed here.
4. Finally, Chapter 5 presents overall conclusions and recommendations for future work.

CHAPTER 2

EXPERIMENTAL MATERIALS

2.1 Experimental Setup

The experimental setup for abiotic testing is shown in Figure 2.1. The solution used for the experiments was 5 mM sodium carbonate prepared using deionized (DI) water and sodium carbonate powder (EMD, USA). The initial pH of the solution was approximately 10.8. The solution was poured into a 500-mL glass bottle (PYREX, Germany). The glass bottle had an additional volume allowance of approximately 200 mL, thus 700 mL of the solution was used to minimize headspace by filling the bottle till its top. A magnetic stir bar and stir plate (Super-Nuova, Thermo Fisher Scientific, USA), set at 600 rpm, were used to ensure well-mixed conditions inside the bottle. The glass bottle was sealed with a lid that was modified to have an opening for a pH probe, and two openings through which the membrane module was inserted to minimize gas exchange with the surrounding air. Polyurethane tubing (Surethane NSF-51, ATP, USA) was used as the connection tubing through which gas was supplied.

Various compositions of gas were used: 100% CO_2, 90% CO_2, 50% CO_2, and 10% CO_2. The balancing gas in the latter three cases was air (~79% N_2 and 21% O_2). The gas was supplied from a gas cylinder (PRAXAIR, USA) with the pressure being controlled by a regulator. The volumetric flow rate, mass flow rate, temperature, and pressure at the inlet and outlet of the system was recorded using flow meters (MC Series,

ALICAT Scientific, USA). The pH of the solution was measured using a glass electrode pH meter (Lab 860 pH meter, Schott Instruments, Germany). Effluent CO_2 was measured using a COZIR-WR 100% CO_2 sensor when the effluent CO_2 was above 30%, and a low-level CO_2 sensor was used below 30% to obtain accurate results. In this case, the relative humidity and temperature of the gas leaving the fiber lumen were measured using digital SH2x and SH3x sensors (Sensirion, Switzerland). For experiments for which the effluent CO_2 was below 30%, a K33 BLG sensor was used to measure CO_2 and relative humidity.

Experiments involved transfer of CO_2 from the fiber lumen to the bulk liquid by its mass transport through the membrane wall and an external diffusion layer. Uptake of CO_2 lowered the pH from the starting value of approximately 10.8, and the experiments were conducted until the pH of the solution dropped to 7. The temperature did not change during the experiments. In order to remove any residual gas present in the lumen of the membranes, the HFM module was flushed and pressurized with the gas being used for that experiment before immersion into the solution.

Off-gassing of dissolved CO_2 from the solution could occur in some conditions simultaneously with CO_2 delivery through the HFM modules. CO_2 off-gassing increased the solution pH. Thus, experiments were conducted to estimate off-gassing rates based on the rate of increase of pH. When the solution pH dropped to 7 due to CO_2 uptake, the HFM module used in delivering CO_2 to the solution was replaced with an identical HFM module not connected to any gas supply. In the absence of CO_2 uptake, off-gassing

resulted in an increase in pH. pH was measured until approximately 8.3, when off-gassing rates significantly diminished. In order to see the effect of stirring on the off-gassing rate, the solution was stirred using a magnetic stir bar in one experiment, and stirring was absent in another experiment.

In experiments to verify the accuracy of the model developed to quantify the CO_2 flux through the membrane module (Chapter 3), samples were taken from the sodium carbonate solution at regular pH intervals so that the DIC could be measured using the TOC-V instrument (Shimadzu Corp., Japan). 15 mL samples were taken in glass falcon tubes after a decrease in pH of 0.25 between the pH range 8 – 10. The samples were diluted with 15 mL of acidified DI water and sealed immediately with Parafilm to slow carbon losses due to off-gassing.

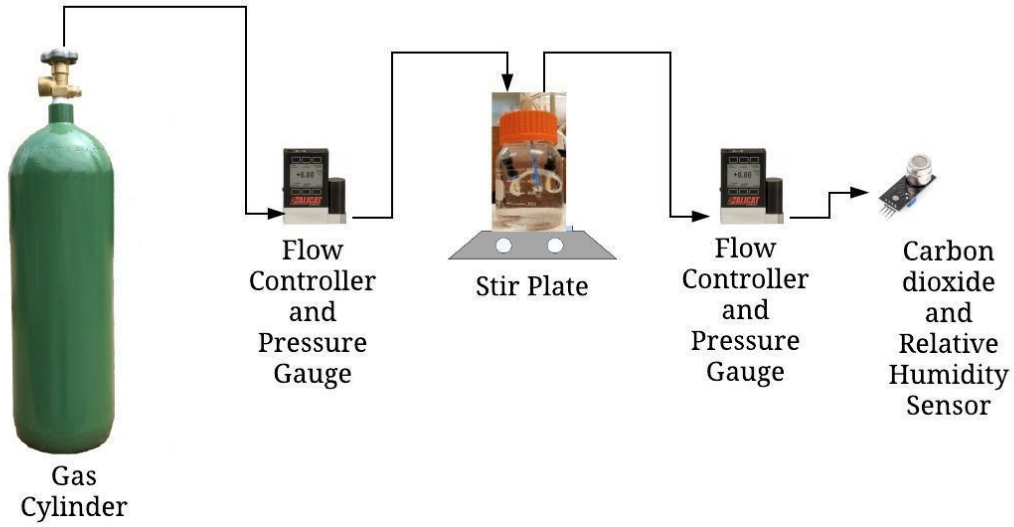

(a)

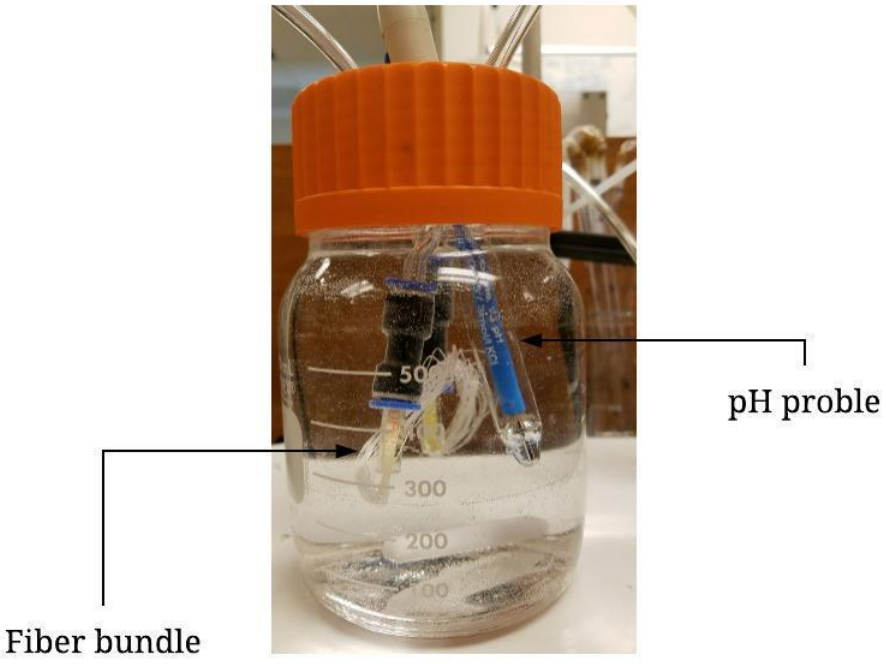

(b)

Figure 2.1. (a) Experimental setup used for abiotic testing; (b) Reactor setup.

2.2 Membrane Characteristics and Assembly into Modules

Two bubbleless hollow-fiber membranes were evaluated: composite and polypropylene membranes. The composite HFM (Model MHF 200TL, Mitsubishi-Rayon Co., Ltd., Japan) consisted of a 1 μm-thick, nonporous polyurethane inner layer sandwiched between two macroporous polyethylene layers, as seen in Figure 2.2. The polyethylene layers are hydrophobic and porous (pore size of 0.1 – 0.15 μm), and they are used for structural support. The dense, nonporous polyurethane layer blocks any continuous pores, allowing for high operating pressures in the lumen, but without bubble formation. The porosity of the composite membrane was about 40%, and the outer diameter and wall thickness were 280 and 40 μm, respectively. The length of the composite HFM varied from 5 – 37 cm. The polypropylene fibers (Teijin Fibers, Ltd., Japan) were single-layered and non-porous. The outer diameter and wall thickness were 200 and 55 μm, respectively (Tang et al., 2012).

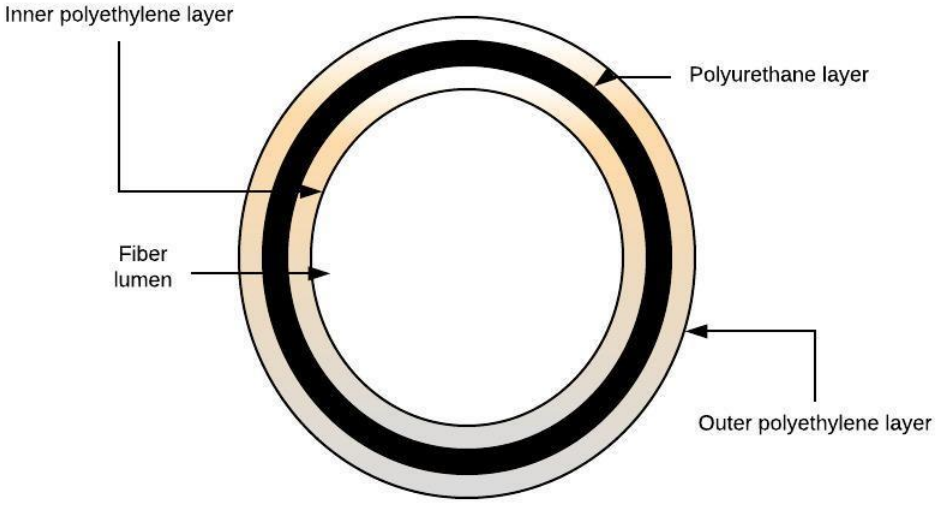

(a)

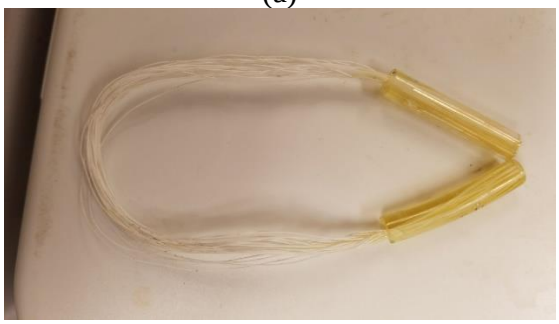

(b)

Figure 2.2. (a) Cross-section of a polyethylene composite HFM; (b) Actual HFM used.

A membrane module was made by potting the ends of the fibers in a small piece of polyethylene tubing and gluing the ends together with urethane adhesive (3M Scotch-Weld 3532 B/A). The tubing was then connected to the gas supply tubing using a push-fit connector. Because the urethane adhesive could pinch some of the fibers, leading to their loss of gas-transfer utility, a liquid resin (Max Bond low viscosity industrial strength adhesive) was used to avoid this problem. A combination of high viscosity resin and high viscosity curing agent were mixed in a 1:1 ratio and added to the polyurethane

tubing used for potting the fibers. This acted as a mold to secure the fibers within the tubing. The high viscosity epoxy was allowed to dry for a maximum of 24 hours. Next, a combination of the thin-set (low viscosity) epoxy was injected into the tubing to plug any air pockets around the fiber ends as can be seen in Figure 2.3 (b). This created an air-tight seal around the fiber ends in the tubing. The low viscosity epoxy was also allowed to dry for 24 hours. A piece of the tubing's end was then cut such that the fiber ends could be exposed to the influent gas stream as shown in Figure 2.3 (a).

(a) (b)

Figure 2.3. (a) Top view of fiber ends; (b) Longitudinal view of fiber ends.

A second glass bottle was set up in the absence of a HFM. In this control setup, CO_2 was delivered to the solution via direct bubbling using a sintered porous stone. The influent flow rate was set at 15 sccm (standard cubic centimeter per minute) to ensure that the time-scale of the experiment was long enough to record sufficient data points. A higher flow rate would result in rapid CO_2 delivery to the solution, resulting in large drops in pH over small time periods. Similar to the setup for a HFM module, the flux and

mass-transfer coefficient for the bubbling system was evaluated using pure CO_2, 90% CO_2, 50% CO_2, and 10% CO_2.

CHAPTER 3

ESTIMATING THE CARBON-DIOXIDE TRANSFER RATES

3.1 Mass-Transfer Coefficient Theoretical Considerations

In a membrane carbonation system, the driving force for CO_2 transfer is provided by a high concentration gradient between the gas and the liquid phase. As the CO_2 gas molecule diffuses from the bulk gas phase to the solution, it experiences resistance at every stage in series. The overall resistance to the rate of transfer of CO_2 over the entire path can be calculated as the sum of the resistances to mass transfer at every stage. For the composite HFM used in this study, the resistances that affect the rate of transfer of CO_2 are shown below in Figure 3.1.

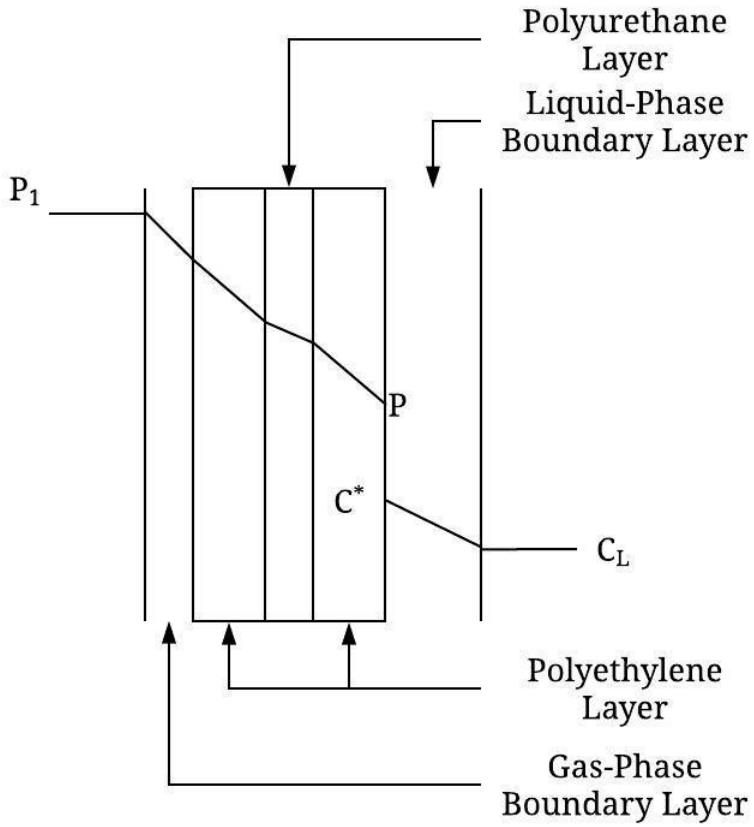

Figure 3.1. Resistances to gas-transfer in a composite HFM.

Since the HFM depicted in Figure 3.1 is hydrophobic, the gas phase and the liquid phase come in contact on the surface of the membrane, since the pores in the macroporous polyethylene layer contain a stagnant gas film. In a hydrophilic HFM, a stagnant liquid layer is present in the pores between the gas phase and the liquid phase. In this case, the gas dissolves in the liquid contained in the pores of the membrane before diffusing into the bulk liquid phase (Kreulen et al., 1993). However, it is possible that the external macropores of the hydrophobic HFM could be water-filled from immersion in solution over long periods of time.

According to two-film theory, the overall resistance to CO_2 transfer from the bulk gas to the liquid solution ($1/K_L$) is the sum of resistances imposed by the gas boundary layer ($1/k_G$), the membrane material ($1/k_M$), and the liquid boundary layer ($1/k_L$),

$$\frac{1}{K_L} = \frac{1}{Hk_G} + \frac{1}{Hk_M} + \frac{1}{k_L} \qquad \textbf{(3.1)}$$

where K_L (m s^{-1}) is an overall mass-transfer coefficient based on liquid-phase concentrations, k_G, k_M, and k_L (m s^{-1}) are mass-transfer coefficients in the gas boundary layer, within the membrane, and in the liquid boundary layer, respectively, and H is the Henry's law constant. Since the Mitsubishi Rayon HFM is comprised of a nonporous polyurethane layer sandwiched between two macroporous polyethylene layers, Equation (3.1) can be expanded to,

$$\frac{1}{K_L} = \frac{1}{Hk_G} + \frac{1}{Hk_{MP}} + \frac{1}{HK_Dk_{NP}} + \frac{1}{Hk_{MP}} + \frac{1}{k_L} \qquad \textbf{(3.2)}$$

where k_{MP} and k_{NP} (m s^{-1}) are mass-transfer coefficients within the macroporous polyethylene layer and nonporous polyurethane layer, respectively, and K_D is the dimensionless distribution coefficient of CO_2 between air and the nonporous layer (Ahmed et al., 2004; Carvalho and Malcata, 2001). Since K_L is based on liquid-side conditions, H and K_D serve as correction factors to represent the resistances or mass-transfer coefficients in terms of the liquid-phase concentrations (Ahmed et al., 2004).

The stage with the highest resistance or lowest mass-transfer coefficient dominates Equation (3.2) and controls the CO_2 transfer rate. The contribution of k_L to the overall mass-transfer coefficient depends on the liquid flow rate. The resistance to mass

transfer in the liquid film decreases with an increase in the liquid flow rate (Ahmed et al., 2004). The mass-transfer coefficient of polyurethane does not change with variations in gas or liquid flow-rates, since it is a function of the nonporous nature of the polyurethane layer. Thus, the contribution of the nonporous layer resistance ($1/K_D k_{NP}$) to the overall resistance is significant. The diffusivity of CO_2 in the gas phase is about 4 orders of magnitude higher than the diffusivity of CO_2 in the liquid phase, suggesting that the liquid film mass-transfer coefficient is much lower than the gas film mass-transfer coefficient (Ahmed and Semmens, 1992b; Carvalho et al., 2006; Carvalho and Malcata, 2001; Ferreira et al., 1998).

The mass-transfer coefficient of the internal macroporous layer can be ignored, since it offers negligible resistance to CO_2 transfer. If the macroporous layer is hydrophobic, the pores contain a stagnant gas layer. As stated earlier, the liquid-film resistance dominates the gas-film resistance, since the diffusivity of CO_2 in the bulk gas-phase is significantly higher. If the macroporous layer is hydrophilic, the pores are filled with a stagnant liquid layer, and CO_2 must dissolve in the membrane before diffusion into the solution. However, the extra resistance term can be ignored since the thickness of the liquid-phase boundary layer is much higher than the diameter of the pores in the macroporous layer of the membrane (Carvalho and Malcata, 2001). This means that CO_2 can diffuse much quicker through the interior pores in the membrane than the liquid-phase boundary layer. However, the external macropores also can be water-filled. Thus, the resistances to gas-transfer through the water-filled external macroporous layer and the liquid-phase boundary layer are lumped together.

For a composite HFM, based on these assumptions, Equation (3.2) can be simplified to,

$$\frac{1}{K_L} \cong \frac{1}{HK_D k_{NP}} + \frac{1}{k_L} \quad \textbf{(3.3)}$$

Equation (3.3) also is applicable for a solid, nonporous membrane, for example, a solid polypropylene membrane. For a macroporous membrane without a nonporous core, as long as bubbles do not form, Equation (3.2) simplifies to,

$$\frac{1}{K_L} \cong \frac{1}{k_L} \quad \textbf{(3.4)}$$

The rate at which CO_2 is transferred from the gas phase to the liquid phase (N_{CO_2}, mol m^{-3} min^{-1}) is proportional to the driving force, i.e., the concentration gradient, and the mass-transfer area. This rate can be calculated by the following simple mass balance:

$$N_{CO_2} = \frac{dC}{dt} = K_L \cdot a \times (C^*_{CO_{2(aq)}} - C_{CO_{2(aq)}}) \quad \textbf{(3.5)}$$

where $K_L \cdot a$ (min^{-1}) is the overall volumetric mass transfer coefficient of CO_2, a denotes the gas-liquid interfacial area per unit volume of liquid, $C_{CO_2,aq}$ (mol L^{-1}) is the concentration of CO_2 dissolved in the bulk liquid, and C^* (mol L^{-1}) is the concentration of CO_2 that would be dissolved in the bulk liquid if the liquid phase were in equilibrium with the CO_2 in the gas phase. $K_L \cdot a$, or the lumped resistances, characterizes the kinetics of CO_2 mass transfer (Carvalho et al., 2006).

3.2 Carbonate Equilibrium, Theoretical Considerations

When gaseous CO_2 dissolves in water, it undergoes three chemical reactions with four chemical species, as shown in Figure 3.2: dissolved CO_2 ($CO_{2(aq)}$), carbonic acid (H_2CO_3), bicarbonate ion (HCO_3^-), and carbonate ion (CO_3^{2-}) (Blanken et al., 2017; Hill, 2006).

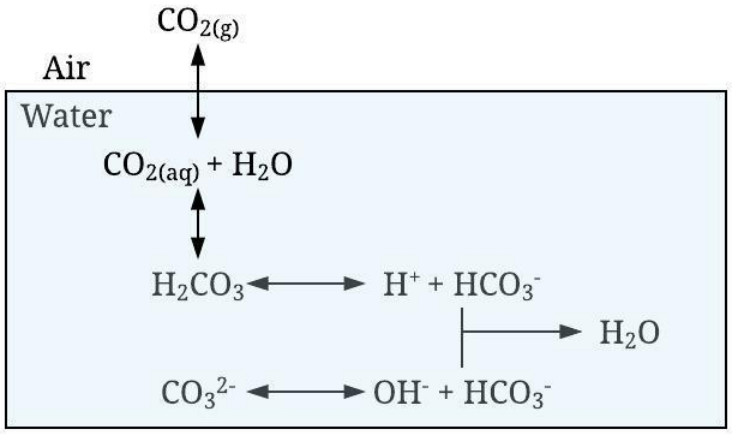

Figure 3.2. Carbon dioxide-bicarbonate-carbonate equilibrium

These equilibria that relate the species are:

$$H_2O_{(l)} + CO_{2(aq)} \overset{K}{\leftrightarrow} H_2CO_{3(aq)} \quad \textbf{(3.6)}$$

$$H_2CO_{3(aq)} \overset{K_1}{\leftrightarrow} HCO^-_{3(aq)} + H^+_{(aq)} \quad \textbf{(3.7)}$$

$$HCO^-_{3(aq)} \overset{K_2}{\leftrightarrow} CO^{2-}_{3(aq)} + H^+_{(aq)} \quad \textbf{(3.8)}$$

$$H_2O_{(l)} \overset{K_W}{\leftrightarrow} H^+_{(aq)} + OH^-_{(aq)} \quad \textbf{(3.9)}$$

where K is the CO_2-hydration equilibrium constant, K_1 and K_2 are equilibrium constants corresponding to the dissociation of H_2CO_3 to its first and second basic species, respectively, and K_W is the ionic product of water dissociation.

When the law of mass action is applied to Equation (3.6), the following equation is obtained:

$$K' = \frac{\{H_2CO_3\}}{\{CO_2\}\{H_2O\}} \quad \textbf{(3.10)}$$

where {x} represents the activity of species x. The activity is the product of the activity coefficient (γ) and the concentration. Due to the low ionic strength of the medium, $\gamma \rightarrow 1$ (Stumm and Morgan, 1996). In dilute aqueous solutions, $\{H_2O\} = 1$. Thus, Equation (3.10) can be simplified to

$$K = K'\{H_2O\} = \frac{[H_2CO_3]}{[CO_2]} \quad \textbf{(3.11)}$$

At 25ºC, K is equal to 650. Equation (3.11) can then be simplified to,

$$[CO_{2(aq)}] = 650\,[H_2CO_3] \quad \textbf{(3.12)}$$

Less than 0.3% of CO_2 reacts with water to form H_2CO_3; thus, the concentration of dissolved CO_2 is much greater than that of H_2CO_3, and a large fraction of un-ionized

CO_2 is present in the form of $CO_{2(aq)}$ (Hill, 2006; Lower, 1999; Stumm and Morgan, 1996). According to convention, the equilibrium mixture, $H_2CO_3^*$, is

$$[H_2CO_3^*] = [CO_{2(aq)}] + [H_2CO_3] \quad \textbf{(3.13)}$$

Due to the low concentration of H_2CO_3 compared to $CO_{2(aq)}$, Equation (3.13) can be approximated as

$$[H_2CO_3^*] \cong [CO_{2(aq)}] \quad \textbf{(3.14)}$$

Substituting Equation (3.13) into Equation (3.12) yields

$$(0.998)\times[H_2CO_3^*] = [CO_{2(aq)}] \quad \textbf{(3.15)}$$

Similar to Equation (3.11), the equilibrium constants for Equations (3.7), (3.8), and (3.9) can be defined as

$$K_1 = \frac{[H^+]\,[HCO_3^-]}{[H_2CO_3^*]} \quad \textbf{(3.16)}$$

$$K_2 = \frac{[H^+]\,[CO_3^{2-}]}{[HCO_3^-]} \quad \textbf{(3.17)}$$

$$K_W = [H^+]\,[OH^-] \quad \textbf{(3.18)}$$

The mass balance equation to compute DIC, or the sum of all the dissolved inorganic carbon species in solution, is

$$C_T = [H_2CO_3^*] + [HCO_3^-] + [CO_3^{2-}] \quad \textbf{(3.19)}$$

If no other acid or base species are present, a charge balance equation or proton condition equation is

$$[H]^+ = [OH^-] + [HCO_3^-] + 2\,[CO_3^{2-}] \quad \textbf{(3.20)}$$

The ionization fractions or α values for H_2CO_3, HCO_3^-, and CO_3^{2-} can be calculated based on Equations (3.16) – (3.20),

$$\alpha_0 = \alpha_{H_2CO_3^*} = \frac{[H^+]^2}{[H^+]^2 + [H^+]\,K_1 + K_1\,K_2} = \frac{[H_2CO_3^*]}{C_T} \quad \textbf{(3.21)}$$

$$\alpha_1 = \alpha_{HCO_3^-} = \frac{[H^+]\,K_1}{[H^+]^2 + [H^+]K_1 + K_1K_2} = \frac{[HCO_3^-]}{C_T} \quad \textbf{(3.22)}$$

$$\alpha_2 = \alpha_{CO_3^{2-}} = \frac{[H^+]\,K_1\,K_2}{[H^+]^2 + [H^+]K_1 + K_1K_2} = \frac{[CO_3^{2-}]}{C_T} \quad \textbf{(3.23)}$$

where the subscript on α represents the number of protons lost from the most protonated species (Stumm and Morgan, 1996). The α values are related by the following equation:

$$\alpha_{H_2CO_3^*} + \alpha_{HCO_3^-} + \alpha_{CO_3^{2-}} = 1 \quad \textbf{(3.24)}$$

Due to the fast conversion of $CO_{2(aq)}$ to HCO_3^-, the effective Henry's law constant (H^{cp*}) seems higher than the value seen for CO_2 alone. Equation (3.41) can be substituted into Equations (3.16) and (3.17) to obtain:

$$[HCO_3^-] = \frac{K_1\,H^{cp}\,P_{CO_2}}{[H^+]} \quad \textbf{(3.25)}$$

$$[CO_3^{2-}] = \frac{K_1\,K_2\,H^{cp}\,P_{CO_2}}{[H^+]^2} \quad \textbf{(3.26)}$$

where H^{cp} is the Henry's law constant relating $[CO_{2(aq)}]$ with the partial pressure of CO_2 (P_{CO_2}). Equations (3.29) and (3.30) can then be substituted into Equation (3.19) to obtain:

$$C_T = H^{cp} P_{CO_2} \left(1 + \frac{K_1}{[H^+]} + \frac{K_1 K_2}{[H^+]^2}\right) \quad \textbf{(3.27)}$$

Since more carbon is dissolved than is expected from Henry's law alone, the effective Henry's law constant can be defined as:

$$H^{cp^*} = H^{cp} \left(1 + \frac{K_1}{[H^+]} + \frac{K_1 K_2}{[H^+]^2}\right) \quad \textbf{(3.28)}$$

$H^{cp^*} > H^{cp}$ because the dissolved carbon dioxide can be stored in the form of bicarbonate or carbonate. If the solution consisted of only $[CO_{2(aq)}]$, then $H^{cp^*} = H^{cp}$. Since carbon speciation in the solution depends heavily on pH, H^{cp^*} at pH > 8 will be significantly higher than H^{cp}. At pH 8 and a temperature of 298 K, the value of H^{cp^*} is 1.5 mol L^{-1} atm^{-1}, and the value of H^{cp} is 0.034 mol L^{-1} atm^{-1}.

3.3 Numerical Model for Flux and Mass-transfer Coefficient

I calculated the overall mass-transfer coefficient ($K_L \cdot a$) from experimental results I obtained from the delivery of CO_2 to a 5-mM Na_2CO_3 solution; the experimental methods are described in Section 2.1. The value of the mass-transfer coefficient was obtained based on the amount of inorganic carbon added in the Na_2CO_3 solution over time. The concentration of DIC present in the solution at t = 0 ($C_{T,0}$) was 0.005 M. The total alkalinity of the solution at t = 0 and for the entire experiment ($[Alk]_0$) was 10 mM. The analytical definition of alkalinity is:

$$[\mathrm{Alk}]_0 = [\mathrm{HCO_3^-}] + 2\,[\mathrm{CO_3^{2-}}] + [\mathrm{OH^-}] - [\mathrm{H^+}] \quad \textbf{(3.29)}$$

Table 3.1 states the values for the constant parameters used in the model.

Table 3.1. Values of the constants in the model.

Parameter	Symbol	Value	Units	Reference
Ionic product of water	K_W	10^{-14}	$mol^2\ dm^{-6}$	(Lower, 1999)
Hydration equilibrium	K	0.0016	−	(Lower, 1999)
First dissociation constant	K_1	6.3	−	(Stumm and Morgan, 1996)
Second dissociation constant	K_2	10.3	−	(Stumm and Morgan, 1996)
Henry's law constant	H^{cp}	0.034	$mol_{gas}\ L_{soln}^{-1}\ atm^{-1}$	(Sander, 2015)
Reactor volume	V	0.7	L	Experimental
CO_2 molecular weight	MW_{CO_2}	44	g/mol	−

I first computed the increase in the total concentration of DIC (C_T) based on the total alkalinity ($[Alk]_0$), which was fixed, and the change in pH over time of CO_2 addition. The concentration of protons in the solution ($[H^+]$) was calculated based on the measured pH of the solution using Equation (3.30).

$$[\mathrm{H^+}] = 10^{-\mathrm{pH}} \quad \textbf{(3.30)}$$

The ionization fractions for $H_2CO_3^*$, HCO_3^-, and CO_3^{2-} ($\alpha_{H_2CO_3^*}, \alpha_{HCO_3^-}, \alpha_{CO_3^{2-}}$) were computed from Equations (3.21), (3.22), and (3.23). C_T was then calculated using Equation (3.31), which was derived by rearranging the analytical definition of alkalinity and substituting Equations (3.18), (3.22), (3.23), and (3.29).

$$C_T = \frac{[Alk]_0 - \frac{K_W}{[H^+]} + [H^+]}{\alpha_1 + 2\alpha_2} \quad \textbf{(3.31)}$$

The mass of CO_2 transferred (m_{CO_2}) in grams present in the solution was then calculated based on C_T and the reactor volume (V), as shown in Equation (3.32).

$$m_{CO_2} = MW_{CO_2} \times C_T \times V \quad \textbf{(3.32)}$$

Having m_{CO_2} and time (t), I could compute the transfer rate of CO_2 (J_{CO_2}) into the solution in units of $gCO_2\ m^{-2}$ per unit time, using Equation (3.33). The surface area (SA) of the membrane module was computed using Equation (3.34) based on the diameter of the HFM (D, m), the length of one fiber (l, m), and the number of fibers used (n). The change in concentration of DIC over time can be calculated using Equation (3.35).

$$J_{CO_2} = \frac{(m_{CO_2})_{i+\Delta t} - (m_{CO_2})_i}{SA \times \Delta t} \quad \textbf{(3.33)}$$

$$SA = \pi n l D \quad \textbf{(3.34)}$$

$$N_{CO_2} = \frac{(m_{CO_2})_{i+\Delta t} - (m_{CO_2})_i}{V \times \Delta t} \quad \textbf{(3.35)}$$

I followed the same methodology to calculate the flux and mass-transfer coefficient of the sparged system. Calculating the mass-transfer interfacial area for a sparged system is more complex. Carvalho and Malcata (2001) provide a set of equations to determine the total transfer area in a plain bubbling system. For a sparging system, the total interfacial area available for mass transfer depends on the size of each bubble, the residence time of the bubbles with the liquid phase, and the influent flow rate as shown in Equation (3.36).

$$A = A_B \times \frac{n_B}{t} \times t_s \quad \textbf{(3.36)}$$

where A_B is the surface area of one bubble, n_B is the number of bubbles produced in a certain time-period, and t_s is the contact time of the bubbles with the liquid phase. The time taken to generate one gas bubble at the surface of the porous stone (t_f), the acceleration due to gravity (g) and the influent gas flow rate (Q_g) are required to calculate the average radius of a single bubble (r), as shown in Equations (3.37) and (3.38).

$$t_f = \frac{191\sqrt{Q_g^{1/5}}}{168g^{3/5}} \quad \textbf{(3.37)}$$

$$r = \sqrt[3]{\frac{3Q_g t_f}{4\pi}} \quad \textbf{(3.38)}$$

Since the influent gas flow rate is constant at 15 sccm, the average radius of a bubble is calculated to be approximately 1.6 mm. This value corresponds to the size of the bubbles observed during the experiment as shown in Figure 1.3 (b) and Figure 3.3.

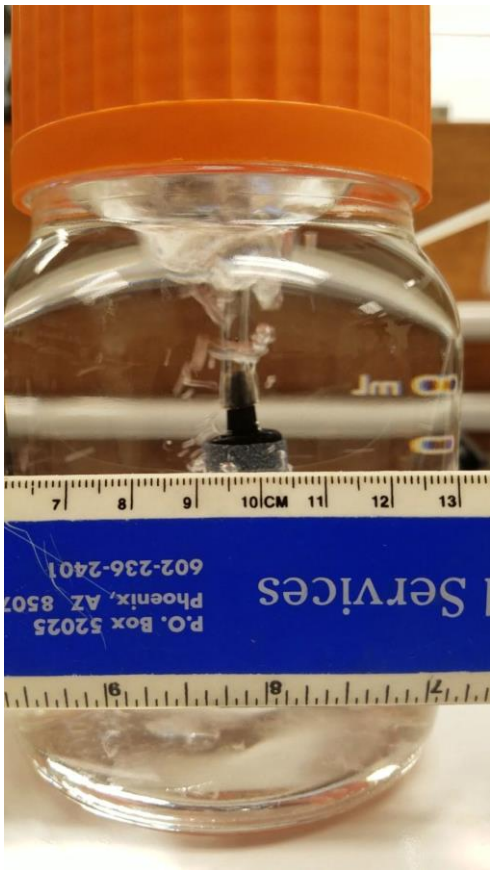

Figure 3.3. Average radius of a bubble in a sparging system.

The contact or residence time depends on the rising velocity (V_t) and the depth at which the porous stone is placed (h) in the glass vessel. The rising velocity is estimated to be about 30 cm/s, and the porous stone is placed at a depth of 7.5 cm from the surface (Baz-Rodríguez et al., 2012). Thus, t_s is estimated to be 0.25 s based on Equation (3.39).

$$t_s = \frac{h}{V_t} \tag{3.39}$$

Based on the pieces of information above, the total interfacial area available for gas transfer in our case is 1.2×10^{-4} m^2.

The driving force for CO_2 transfer (ΔC) is based on the measured dissolved CO_2 concentration ($C_{CO_{2(aq)}}$) and the CO_2 concentration in the liquid phase that would equilibrate the gas phase ($C^*_{CO_{2(aq)}}$). $C_{CO_{2(aq)}}$ can be calculated using Equations (3.15) and (3.21). The partial pressure of CO_2 (P_{CO_2}) can be computed using the composition of CO_2 used in the inlet stream and the pressure of the gas supplied, as shown in Equation (3.40).

$$P_{CO_2} = \%CO_2 \times P \quad \textbf{(3.40)}$$

Equation (3.41) shows that $C^*_{CO_{2(aq)}}$ can be calculated using Henry's law.

$$C^*_{CO_{2(aq)}} = H^{cp} \times P_{CO_2} \quad \textbf{(3.41)}$$

Having C_T and N_{CO_2}, I was able to compute $K_L{\cdot}a$ using the mass balance in Equation (3.5) and K_L from Equation (3.42), assuming that the only process occurring was the transfer of CO_2 from the gas phase to the liquid phase.

$$K_L = \frac{J_{CO_2}}{\Delta C} \quad \textbf{(3.42)}$$

The gas-liquid interfacial area per unit volume (a) can then be computed from Equation (3.43), which gives an idea as to how much surface area is available for mass transfer since the reactor volume is constant. Because CO_2 could off-gas if CO_2 became a significant species of C_T, I utilized the C_T and CO_2 values only for pH $\geq$ 8.

$$a = \frac{K_L a}{K_L} \tag{3.43}$$

3.4 Results and Discussion

I evaluated two HFMs using the model described in Section 3.3: a Mitsubishi-Rayon HFM composed of two macroporous polyethylene layers and a nonporous polyurethane layer, and a nonporous polypropylene membrane. As shown in Figure 3.4, the former delivered CO_2 at a much faster rate than the polypropylene membrane based on the rate of pH reduction. The thick nonporous layer in the polypropylene membrane added significant resistance to mass transfer. Thus, the Mitsubishi-Rayon HFM was evaluated for the remainder of the experiments.

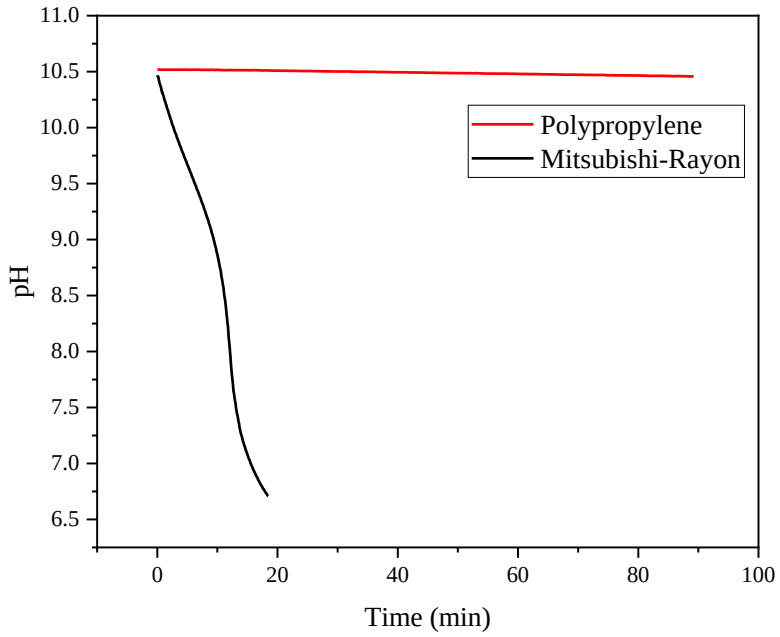

Figure 3.4. The plots of pH versus time for non-porous polypropylene and composite Mitsubishi-Rayon HFMs in a closed system with delivery of pure CO_2.

To evaluate the accuracy of the model, I conducted special experiments to compare the predicted concentrations of DIC with the measured DIC values. Figure 3.5 shows the comparison. In Figure 3.5 (b), all measured DIC concentrations are underestimates, as compared to predicted values. The method the Shimadzu instrument utilizes to measure DIC concentration requires samples to be diluted with acidified DI water. Acidified DI water reduces the pH of the samples, which results in off-gassing of dissolved CO_2. Additionally, the time-delay associated with analyzing each sample exacerbated this effect. When I diluted the samples with DI water, the predicted DIC concentrations matched up with measured values as shown in Figure 3.5 (a).

Acidified DI water must be used to dilute the samples in order to run them through the Shimadzu TOC instrument, since DI-water dilution reduces the lifetime of the catalyst used in the instrument. Thus, an advantage of using the model to convert pH to C is that it can provide flux and mass-transfer coefficient values instantaneously.

Figure 3.5 (a) and (b) show deviations between predicted and measured DIC concentrations at a pH of roughly 7. This was due to CO_2 off-gassing as the pH decreased to where CO_2 was the dominant DIC species. Lowering the pH caused the liquid's CO_2 concentration to be super-saturated compared to its concentration in equilibrium with atmospheric CO_2 (~400 ppm). The model does not account for any CO_2 absorbed from or released into the atmosphere at high pH. Thus, the model is inaccurate if the atmosphere becomes a sink for super-saturated CO_2 or a source of CO_2. For this reason, the pH range I used for computing K_La was from 10 to 8, where the rate of CO_2 off-gassing or in-gassing was insignificant, making model-predicted DIC values accurate, as shown in Figure 3.5 (a).

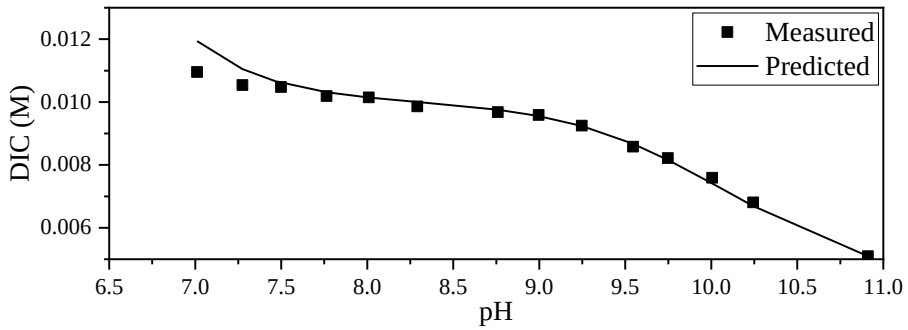

(a)

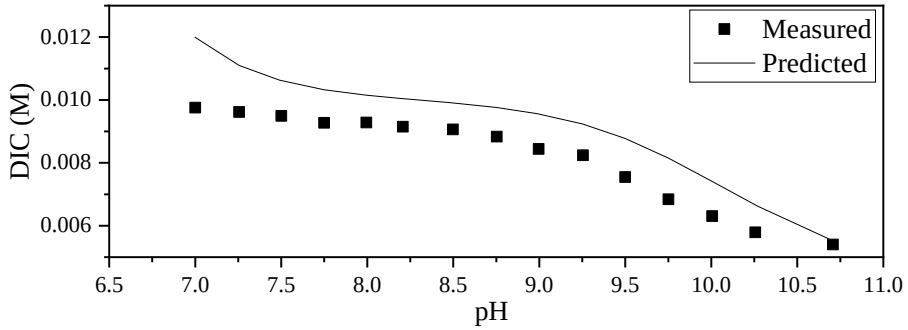

(b)

Figure 3.5. Comparison of DIC concentrations predicted by the model versus measured values using open-end HFM modules of (a) 32 fibers, 0.18 m in length supplied with 90% CO_2 and diluting samples with DI water; (b) 64 fibers, 0.39 m in length supplied with 90% CO_2 and diluting samples with acidified DI water.

Off-gassing occurs at low pH when the concentration of dissolved CO_2 increases drastically, as shown in Figure 3.6. As the pH decreases, CO_3^{2-} is converted into HCO_3^- till the first equivalence point is reached. When the pH is decreased below this point, the concentration of HCO_3^- remains constant due to the assumption of constant total alkalinity employed in the model. 10 mM of alkalinity is conserved in the form of bicarbonate. However, since the CO_3^{2-} initially present in the solution is consumed and

CO_2 is continuously added into solution, the ionization fraction of HCO_3^- decreases, as shown in Figure 1.2. Figure 3.6 shows that the concentration of dissolved CO_2 increases significantly when the pH decreases below 7.5. This corresponds to Figure 3.5, which shows that the measured DIC values begin to deviate from the model-predicted values at a pH of approximately 7.5 due to an increase in the rate of CO_2 off-gassing. This suggests that an increase in the concentration of dissolved CO_2 leads to an increase in the driving force for CO_2 off-gassing.

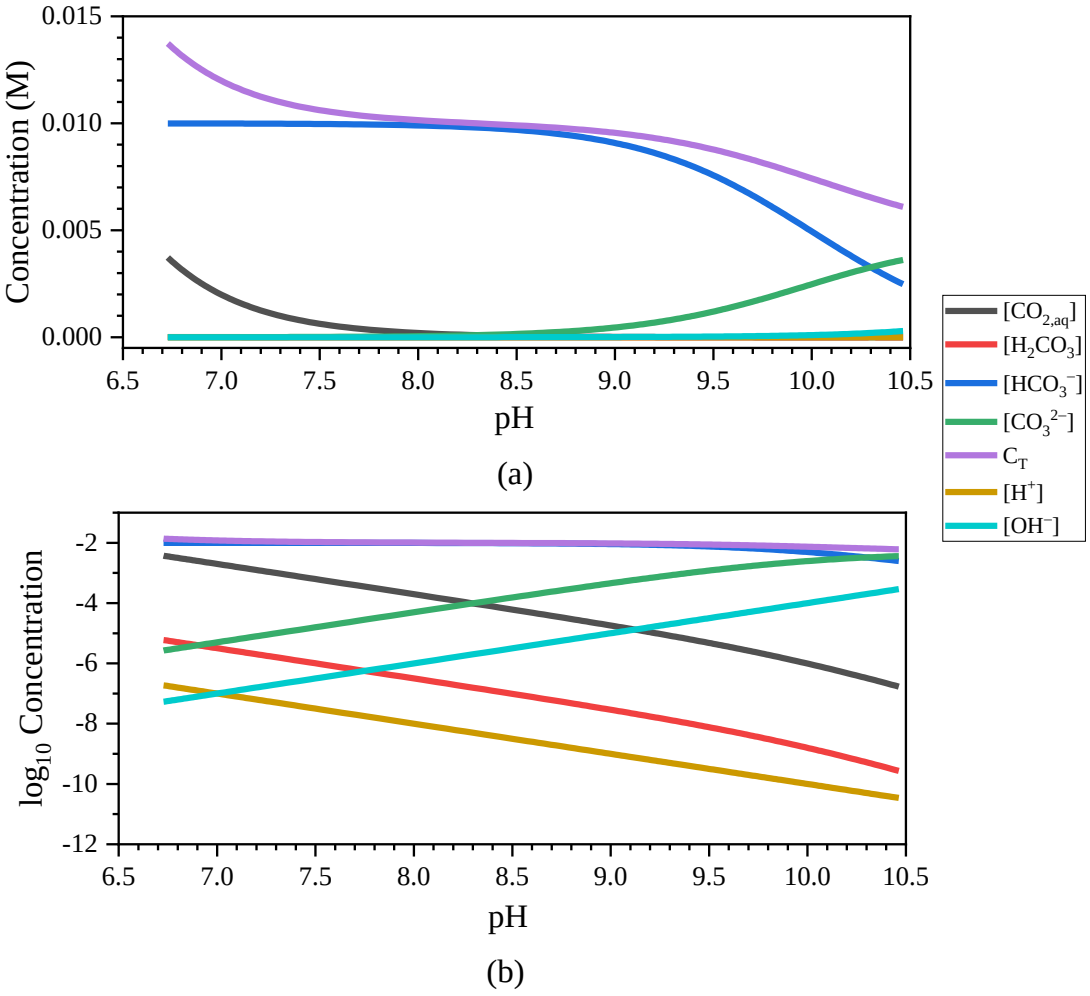

Figure 3.6. Change in the concentration of all species present in solution as the pH decreases with CO_2 addition for an open-end HFM module with 32 fibers, 0.18 m in length supplied with 100% CO_2.

Figure 3.7 shows the effect of pH on the rate of CO_2 loss to the atmosphere. The HFM module used in this experiment was not pressurized with CO_2; thus, CO_2 could have been lost from the top of the surface of the solution, which was exposed to the

atmosphere. Figure 3.7 shows that the rate of CO_2 loss decreased till the equilibrium pH was reached. The rate of CO_2 off-gassing also depended on the hydrodynamic conditions in the reactor. If a more turbulent regime was present in the reactor, the rate of CO_2 loss increased, since a higher liquid surface area was available per unit volume for mass transfer of CO_2 from the aqueous phase to the atmosphere. Additionally, an increase in the liquid-phase velocity decreased the gas-liquid interface resistance to transfer of CO_2 into the gas phase. The effect of stirring the solution can be seen on the rate of CO_2 loss (J) and K_La in Figure 3.7, which shows values calculated using the model. The K_La in the presence of stirring is 20.7 hr^{-1}, a value nearly 5-fold higher than the K_La in the absence of stirring, which is estimated to be 4.5 hr^{-1}. The overall rate of CO_2 loss in the presence of stirring was 170 g m^{-2} day^{-1}, compared to 100 g m^{-2} day^{-1} in the absence of stirring. As shown in Figure 3.7(b), CO_2 loss to the atmosphere was more significant at a lower pH, as the rate of loss was almost zero for pH > 8.

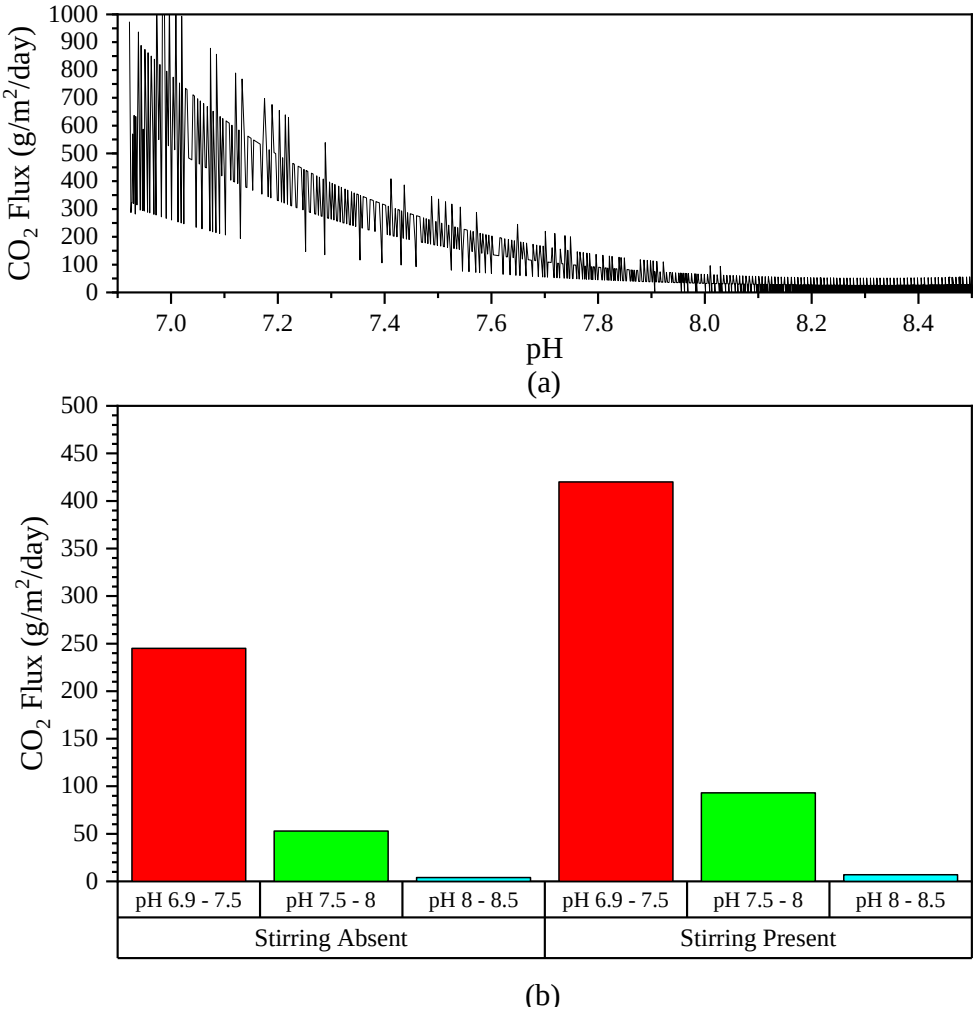

Figure 3.7. (a) Change in the rate of CO_2 loss with a decrease in pH; (b) Rate of CO_2 loss in three pH ranges: 6.9 – 7.5, 7.5 – 8, and > 8.

3.5 Closed-end versus Open-end

The CO_2 concentration decreases in the fiber lumen further away from the source of gas supply in a closed-end membrane module, even when pure CO_2 is fed to the lumen. This is due to the diffusion of inert gases from the solution into the lumen. As a

result, the distal end of the membrane lumen loses its ability to transfer CO_2 to the liquid. Due to the presence of a non-uniform gas concentration profile in the lumen, the average CO_2 flux out of the fibers is reduced. The impact of inert gases is more pronounced when the input gas is less than 100% CO_2, because inert gases in the input stream are selectively retained and concentrated.

In contrast, an open-end membrane module has a high gas velocity in the lumen. Thus, bulk mass transport through the lumen overwhelms diffusive mass transport across the membrane wall and into the solution. This allows for a uniform CO_2-concentration profile to be maintained in the membrane lumen, allowing for CO_2 diffusion to occur throughout the lumen, since any inert gases are vented out. Depending on the partial pressure in the lumen, inert gases can either diffuse into the solution, or back-diffusion can occur. In either case, CO_2 flux across the membrane is reduced. Thus, venting inert gases using an open-end module can improve CO_2 flux, as shown in Figure 3.8. It is important to note that the measured DIC values shown in Figure 3.8 were subject to the acidification problem highlighted earlier. Nevertheless, the trend exhibited by the measured DIC values and the model-predicted values are similar, suggesting that open-end HFMs had a higher CO_2 transport rate than closed-end HFMs.

The disadvantage of an open-end module is that a 100% CO_2 transfer efficiency cannot be achieved, since a large amount of CO_2 is vented. Thus, a closed-end module is characterized by a high CO_2 transfer efficiency, but low CO_2 flux rates, while the opposite trend occurs for an open-end module.

Table 3.2 clearly illustrates the flux trend, particularly for pH 10 – 8, where CO_2 off-gassing was not significant.

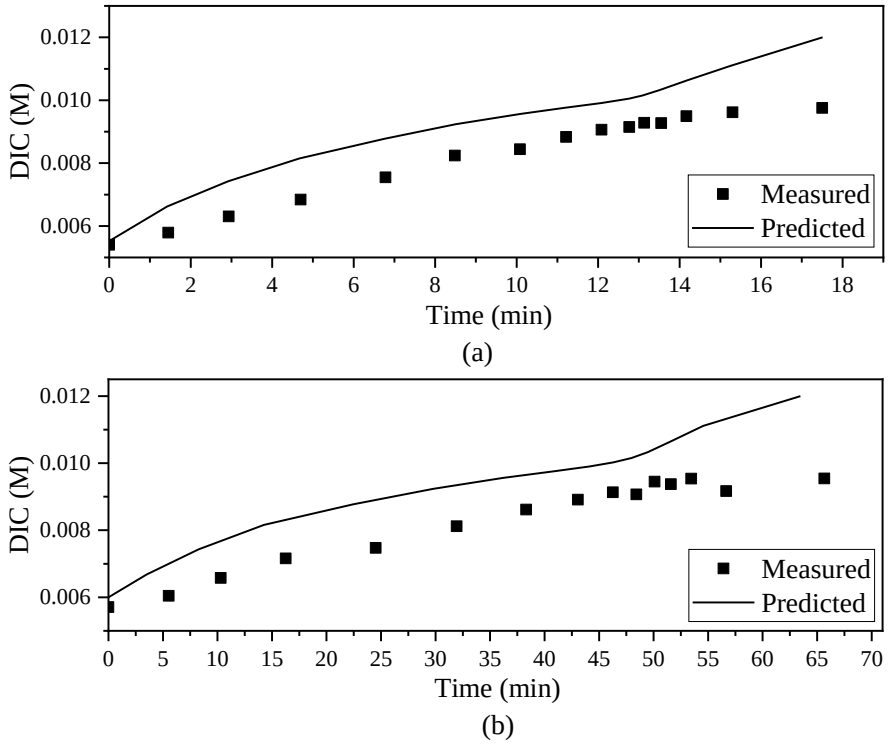

Figure 3.8. Rate of increase in DIC concentrations using 90% CO_2 and a HFM module consisting of 32 fibers, 0.18 m in length operated in (a) open-end mode for 18 minutes; (b) closed-end mode for 70 minutes.

Table 3.2. Comparing predicted and measured CO_2 fluxes between pH 10 – 8, and overall values for a module consisting of 32 fibers, 0.18 m in length operated in open-end mode and closed-end mode, and supplied with 90% CO_2.

Operating Condition	**Overall Flux ($g\ m^{-2}\ day^{-1}$)**		**pH 10 – 8 Flux ($g\ m^{-2}\ day^{-1}$)**	
	Measured	Predicted	Measured	Predicted
Open-end	2000	2500	2200	2000
Closed-end	690	790	590	640

3.6 Pressure Dependence of CO_2 Flux

The pressure dependence of CO_2 flux is shown in Figure 3.9. Higher CO_2 partial pressures increased the driving force for mass transfer. A uniform CO_2 concentration profile can be obtained in the membrane lumen at higher pressures due to an increase in the intra-membrane gas velocity. Figure 3.9 shows that the pressure dependence of CO_2 flux was more significant when pure CO_2 is supplied. An open-end membrane experienced a large pressure drop since the gas flow rate through the membrane was large. For CO_2 supplied with a pressure of 10 psig, the pressure of the effluent gas was close to atmospheric pressure or 0 psig. In contrast, a closed-end module has a negligible pressure drop, resulting in the fiber lumen being pressurized with CO_2. For 50% CO_2, the buildup of inert gases dominated in a closed-end membrane, leading to lower fluxes across the membrane wall. When supplied with CO_2-enriched air, open-end modules performed better than closed-end modules, because inert gases in the lumen were vented

out the distal end. Thus, for a mixed gas, an open-end HFM had a higher average CO_2 partial pressure in the lumen than a closed-end HFM, which provided a larger driving force for mass transfer.

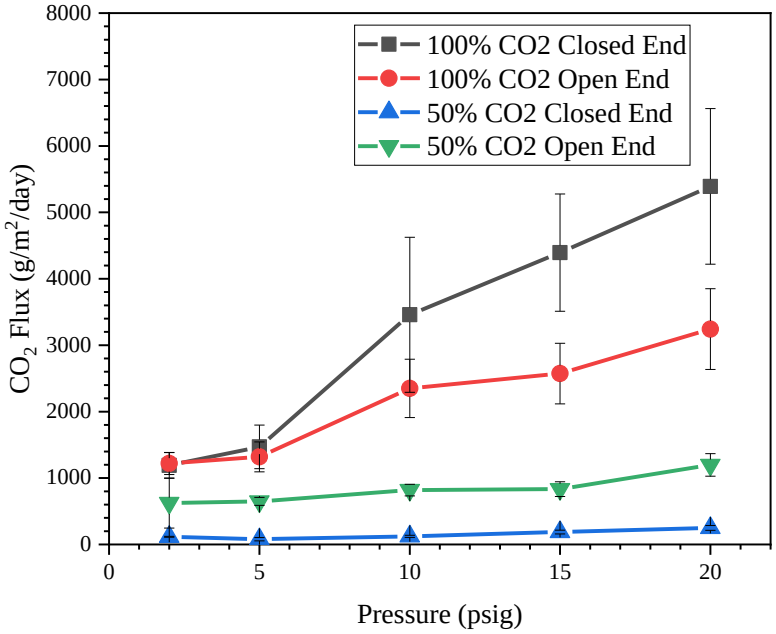

Figure 3.9. CO_2-pressure dependence of CO_2 flux in the pH range 10 – 8. Membrane module used consists of 96 fibers, 0.21 m in length. Error bars represent the standard deviation of data.

3.7 Effect of Inlet CO_2 Concentration on CO_2 Flux

The effect of the amount of CO_2 present in the gas supplied on HFM transfer rates is shown in Figure 3.10. As expected, the CO_2 flux decreased as the concentration of

CO_2 in the inlet stream was lowered due to a decrease in the driving force for mass transfer. Figure 3.10 shows that, for CO_2-enriched air, an open-end HFM performed better than a closed-end HFM in terms of CO_2 flux. This was due to the accumulation of inert gases in the fiber lumen in the closed-end mode, resulting in a decrease in the average lumen CO_2 partial pressure, even though the total pressure was constant. In an open-end HFM, inert gases in the lumen were vented through the distal end of the fiber. Thus, in open-end mode, a more uniform CO_2 concentration profile could be maintained.

For open-end and closed-end modules, CO_2 transfer rates decreased as the concentration of inert gases in the supply stream increased. The mass-transfer rates of inert gases, in this case, were higher, which reduced CO_2 flux across the membrane. For pure CO_2, closed-end mode performed better than open-end mode. This is because the effect of the pressure drop in open-end mode was larger than the buildup of inert gases in closed-end mode.

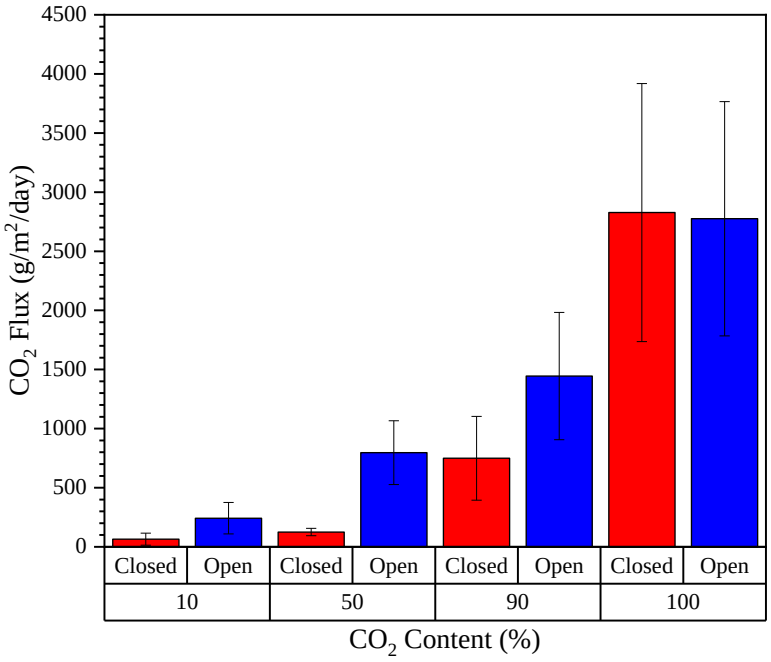

Figure 3.10. Effect of inlet CO_2 composition on flux evaluated at 10 psig. Data presented are the average of multiple HFM modules. Error bars represent the standard deviation of data.

The transfer rates obtained using a sparging or bubbling system were significantly higher than those obtained from a HFM, as shown in Figure 3.11. For pure CO_2, a flux of approximately 200,000 g m^{-2} day^{-1} was obtained for the bubbling system compared to approximately 2500 g m^{-2} day^{-1} for a HFM. The average K_La value obtained for a sparging system was 0.59 ± 0.03 hr^{-1}. The total interfacial mass-transfer area was found to be 1.2×10^{-4} m^2 using Equation (3.36). Based on this area, the specific interfacial area is determined to be 0.17 m^{-1} for a volume of 700 mL. Carvalho and Malcata, 2001 obtained a K_La and a value of 0.42 hr^{-1} and 1.05 m^{-1} respectively, using a mass-transfer

area of 1.1×10^{-3} m^2. The average K_L value was 0.095 ± 0.005 cm s^{-1}. It makes more sense to compare K_L values instead of K_La because the latter depends on the interfacial mass-transfer area chosen by the researcher, which could vary. A K_L value of 0.0111 cm s^{-1} was obtained by Carvalho and Malcata, 2001, and (0.0583 – 0.0588) cm s^{-1} by Talbot et al., 1991.

K_L was relatively constant for varying inlet CO_2 content, since the hydrodynamic conditions were the same for each reactor. K_La also was relatively constant for each case, indicating that the interfacial area available for mass transfer did not change for a sparging system based on the inlet CO_2 content. K_La was slightly higher for 90% CO_2 due to experimental variability. The size of the bubbles produced, the contact time or the rising velocity, and the flow-rate affect the interfacial mass-transfer area more significantly (Fan et al., 2008). If the bubble diameter is reduced, the ratio of the bubble's surface area to its volume, or the specific exchange area (A/V), will increase based on Equation (3.44). This will increase the value of a.

$$\left(\frac{A}{V}\right)_{BC} = \frac{3}{r} \qquad \textbf{(3.44)}$$

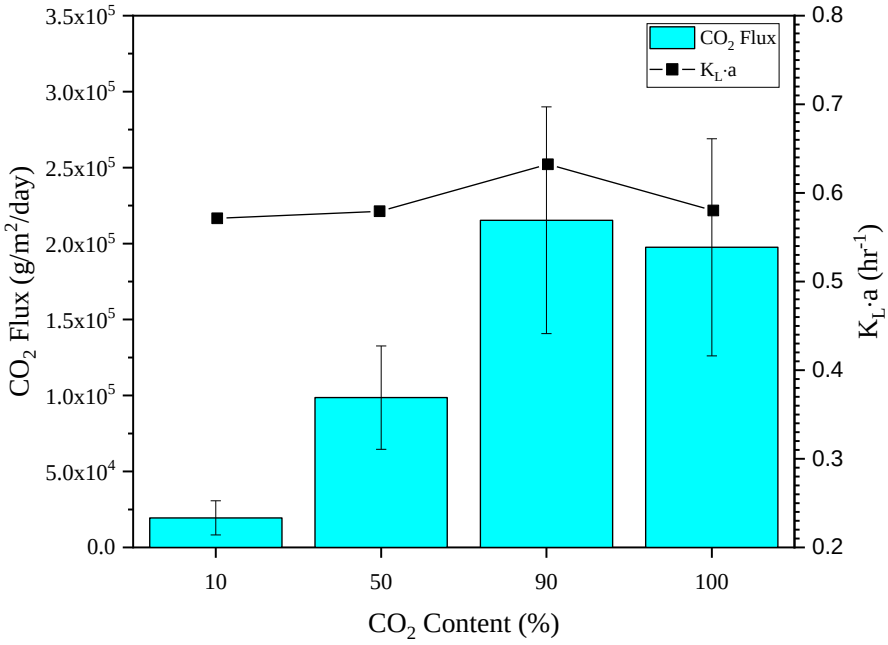

Figure 3.11. Effect of inlet CO_2 gas content on K_La and CO_2 flux for a sparging system operating at a flow rate of 15 sccm and a pressure of 10 psig. Data presented are in the pH range 10 – 8. Error bars represent the standard deviation of flux data.

The values of overall mass-transfer coefficient (K_L), overall volumetric mass-transfer coefficient (K_La), and the interfacial area per unit reactor volume (a) for the composite HFM are shown in Table 3.3. K_L depended only on the polyurethane layer resistance and the liquid-phase boundary layer resistance. The latter can be reduced if the liquid-phase velocity is increased by increasing the stirring rate. However, since the liquid-phase velocity is held constant for each experiment, K_L was constant. Thus, the average K_L for the composite HFM based on the values in Table 3.3 was $(1.31 \pm 0.12) \times 10^{-3}$ cm s^{-1}. An exact comparison of the K_L value obtained here with other reported

values is difficult, since data on CO_2 transfer across a HFM are limited; however, data on O_2 transfer characteristics are abundant. Since the diffusion coefficient of O_2 is higher than that of CO_2, the mass-transfer coefficient of CO_2 will be lower than that of O_2 by a factor of 0.91 (Fan et al., 2008).

Table 3.3. Mass transfer coefficient and interfacial area values for HFM modules supplied with pure CO_2 at 10 psig.

CO_2 Content (%)	Operating Condition	No. of Fibers	Fiber Length (m)	$K_L \times 10^3$ (cm s^{-1})	K_La (hr^{-1})	a (m^{-1})
100	Closed-end	32	0.13	1.27	0.239	5.23
100	Closed-end	32	0.17	1.24	0.306	6.84
100	Closed-end	32	0.18	1.21	0.314	7.24
100	Open-end	32	0.13	1.39	0.261	5.23
100	Open-end	32	0.17	1.51	0.373	6.84
100	Open-end	32	0.18	1.24	0.324	7.24

The K_L value obtained here was consistent with values reported by Ferreira et al. (1998) for microporous polypropylene membranes. They reported K_L values in the range $(1.26 – 2.64) \times 10^{-3}$ cm s^{-1}. Perez-Calleja et al. (2017) used a K_L value of 5.4×10^{-3} cm s^{-1} for evaluating oxygen transfer characteristics in a composite HFM which equates to a K_L of 4.91×10^{-3} cm s^{-1} for CO_2. This is higher than the value reported here since Perez-Calleja et al. (2017) evaluated K_L for a single fiber. The presence of closely packed fibers could increase resistance to mass-transfer since fiber-fiber contact reduces the effective membrane surface area available for mass transfer (Johnson et al., 1997).

The values of a reported in Table 3.3 are based on the overall membrane area as opposed to the membrane area covered by the macropores. Even though the gas-liquid interface is immobilized at the surface of the pores, a thin liquid layer present on the membrane surface is saturated with CO_2. Mass-transfer rates depend on the resistance of this liquid layer. Thus, the membrane area used is the overall membrane area, and not just the surface area covered with pores. K_L and K_La values for open-end modules were higher than those for closed-end modules. This suggests that, due to the buildup of inert gases, the effective membrane area used was less than the maximum membrane area available for mass transfer for a closed-end module. In other words, the value of a actively used was less than the geometric a calculated from the area of the fiber in the closed-end mode. This trend is analyzed in the next two paragraphs.

Model-derived K_L values were lower for a closed-end HFM than an open-end HFM for CO_2-enriched air, as shown in Table 3.4. This was an artifact of the model as K_L should be constant, since it is a function of the nonporous layer and the liquid-phase boundary layer. K_L is independent of the mode of operation. A decrease in the effective membrane interfacial area (a) would be reflected in decreased model-derived K_L values. Alternatively, it was possible that the resistance of interior porous layer and diffusion layer was of important. So, the higher gas velocities prevalent in open-end mode decreased the mass transfer resistance on the inside. This was then reflected by a larger K_L.

The maximum utilizable a for the membrane in Table 3.4 was 7.24 m^{-1}. This value was used in Equation (3.42) to calculate the K_L values shown in Table 3.4. In order to compute the effective a from Equation (3.43), K_L was assumed constant at 1.31×10^{-3} cm s^{-1} from the experiments conducted with pure CO_2. Subsequently, the fiber length used was calculated from Equation (3.34). The effective a and fiber length were lower for closed-end mode than open-end mode due to decreasing CO_2 partial pressures and build-up of inert gases in the lumen. Due to the same reason, the effective a and fiber length also decreased as the CO_2 concentration in the supply gas decreased.

Table 3.4. CO_2 transfer and HFM membrane characteristics using a module consisting of 32 fibers, 0.18 m in length supplied with gas at 10 psig.

CO_2 Content (%)	Operating Condition	Flux ($g\ m^{-2}\ day^{-}$)	$K_L \times 10^4$ ($cm\ s^{-1}$)	K_La (hr^{-1})	Effective a (m^{-1})	Used Fiber Length (m)	(%)
90	Closed	754	4.0	0.103	2.18	0.05	30
90	Open	2149	12.3	0.321	6.81	0.17	94
50	Closed	165	1.6	0.041	0.86	0.02	12
50	Open	1199	11.4	0.296	6.28	0.16	87
10	Closed	53	1.6	0.041	0.86	0.02	12
10	Open	199	9.5	0.233	4.94	0.12	68

Based on Equation (3.44), the specific exchange area for the sparging system was 1880 $m^2\ m^{-3}$. Similar to Equation (3.44), Equation (3.45) was developed for a HFM. Thus, the specific exchange area for a HFM depends solely on the fiber diameter. For the Mitsubishi Rayon HFM, the specific exchange area was 14,300 m^2/m^3 from Equation (3.45), while the sparging system had a specific exchange area of 1880 m^2/m^3. The K_L obtained for a HFM was several orders of magnitude lower than the K_L for the sparging

system, however, the K_La values obtained were very similar. This suggests that the increased resistance to mass transfer in a HFM can be overcome by a higher interfacial area, yielding better K_La values than a sparging system.

$$(\frac{A}{V})_{HFM} = \frac{4}{D} \quad \textbf{(3.45)}$$

CHAPTER 4

MASS BALANCE AND MODEL DEVELOPMENT

4.1 Numerical Mass-balance Model for Intra-Membrane Gas Concentration Profiles

Closed-end HFMs provide the benefit of high transfer efficiency, but can suffer from poor transfer rates; in contrast, open-end HFMs are characterized by high transfer rates, but low transfer efficiencies. By operating a HFM in partially open mode, i.e., restricting the effluent gas flow, it should be possible to attain higher transfer rates than closed-end systems and better transfer efficiencies than open-end systems. The trends in CO_2-transfer efficiency are explored in this chapter.

The model developed in Chapter 3 calculated the CO_2 flux and mass-transfer coefficient across the membrane into the liquid phase based on the measured rate of change of pH and DIC. The rate of mass transfer depended on the mode of operation of the membrane and the concentration of CO_2 supplied. Another factor that could affect membrane performance is the length of each fiber. In order to compare membrane performance for varying HFM surface areas and CO_2 concentrations, I constructed a mass balance on each module to determine the amounts of CO_2, N_2, O_2, and H_2O entering and leaving the system. CO_2-transfer efficiencies were then calculated using the mass balance.

As shown in Table 3.4, the mode of operation and CO_2 concentration affected the membrane interfacial area used for CO_2 mass-transfer. Since the mass balance provides a macroscopic perspective of a HFM, I developed a mass-transport model to understand gas behavior inside the lumen as a function of fiber length, CO_2 concentration, and mode of operation. This provided information on the efficiency of mass-transfer area usage for various parameters.

As shown in Figure 4.1, the inputs into the inlet end of the HFM were CO_2, O_2, and N_2. No water vapor entered the HFM through the inlet, since dry gas was supplied. CO_2 diffused across the membrane wall into the liquid phase. CO_2 flux was calculated using the model described in Chapter 3. N_2 and O_2 could diffuse in or out of the membrane, depending on the partial pressure of these inert gases inside the lumen. If the partial pressure of the inert gases in the lumen exceeded that in the liquid phase, then N_2 and O_2 diffused into the liquid phase similar to CO_2. Otherwise, N_2 and O_2 diffused into the lumen from the liquid phase. In either case, inert gases accumulated in the lumen due to their poor aqueous solubility compared to CO_2. In addition to inert gases, water vapor diffused across the membrane, since dry gas was supplied to the HFM, resulting in a high driving force for H_2O transport into the lumen.

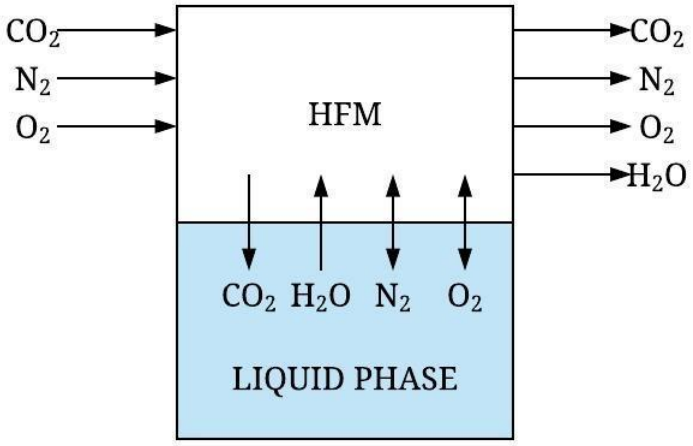

Figure 4.1. Gas inputs and outputs into a HFM considered for the mass balance.

The ALICAT flow meters measured the volumetric flow rates ($\dot{V}$, sccm) and pressures (P, Pa) at the inlet and outlet of the fibers. In all the experiments for the mass balance, gas was supplied at 10 psig. The ALICAT flow meters were used to control the effluent flow rate for partially open-end modules and to prevent any gas outflow for closed-end modules. The temperature of the solution was measured and was constant throughout the experiment. The temperature of the gas in the lumen was assumed to be equal to that of the solution, since there was no temperature change in the solution.

In addition to Table 3.1, additional values for constant parameters are provided in Table 4.1.

Table 4.1. Values of the constants in the model.

Parameter	Symbol	Value	Units	Reference
Gas Constant	R	8.314	J mol^{-1} K^{-1}	–
N_2 Henry's law constant	$H_{N_2}^{cp}$	0.00061	mol L^{-1} atm^{-1}	(Sander, 2015)
O_2 Henry's law constant	$H_{O_2}^{cp}$	0.0013	mol L^{-1} atm^{-1}	(Sander, 2015)
N_2 molecular weight	MW_{N_2}	28	g mol^{-1}	–
O_2 molecular weight	MW_{O_2}	32	g mol^{-1}	–
H_2O molecular weight	MW_{H_2O}	18	g mol^{-1}	–
Overall mass-transfer coefficient for CO_2, N_2, and O_2 transfer	K_L	1.31×10^{-5}	m s^{-1}	Experimental
Overall mass-transfer coefficient for H_2O transfer	K_P	1.49×10^{-6}	mol m^{-2} Pa^{-1} min^{-1}	Experimental
Antoine's equation constants	A	16.3872	–	(Smith et al., 2005)
	B	3885.7	–	
	C	-42.98	–	

The volumetric flow rates at the inlet measured by the ALICAT flow meters were converted into molar fluxes ($\dot{N}$, mol m^{-2} min^{-1}). For this calculation, the partial pressures of CO_2, N_2, and O_2 at the inlet were needed. For pure CO_2, the inlet partial pressures of N_2 and O_2 were 0. For CO_2-enriched air, the balance air was assumed to be composed of 79% N_2 and 21% O_2. The partial pressure of each gas in the inlet stream was calculated using:

$$P_{CO_2,in} = \%CO_{2,in} \times P_{tot,in} \quad \textbf{(4.1)}$$

$$P_{N_2,in} = 0.79(1 - \%CO_{2,in}) \times P_{tot,in} \quad \textbf{(4.2)}$$

$$P_{O_2,in} = 0.21(1 - \%CO_{2,in}) \times P_{tot,in} \quad \textbf{(4.3)}$$

After the partial pressures of each inlet gas were calculated, the molar fluxes of each gas were calculated using the ideal gas law:

$$\dot{N}_{CO_2,in} = \frac{\dot{V}_{in} \times P_{CO_2,in}}{R \times T \times A} \quad \textbf{(4.4)}$$

$$\dot{N}_{N_2,in} = \frac{\dot{V}_{in} \times P_{N_2,in}}{R \times T \times A} \quad \textbf{(4.5)}$$

$$\dot{N}_{O_2,in} = \frac{\dot{V}_{in} \times P_{O_2,in}}{R \times T \times A} \quad \textbf{(4.6)}$$

where A is the cross-sectional area of the membrane, R is the universal gas constant (8.314 J mol^{-1} K^{-1}), and T is the measured gas temperature.

$$A = \frac{\pi}{4} D^2 \quad \textbf{(4.7)}$$

The total molar flux entering the module ($\dot{N}_{tot,in}$) is the sum of the molar fluxes of each gas.

The CO_2 flux across the membrane wall was calculated using the model developed in Chapter 3. The flux calculated using Equation (3.33) was then converted into a molar flux.

$$\dot{N}_{CO_2,\,flux} = \frac{J_{CO_2}}{MW_{CO_2}} \tag{4.8}$$

N_2 and O_2 also diffuse across the membrane wall. The fluxes for both were calculated using Fick's law. K_L depended only on the liquid-phase boundary layer and gas-diffusion across the membrane material. The molecular size of the gas species diffusing across the membrane should affect the K_L value for that species. However, for the gas species in this system, the molecular sizes of N_2 (1.55 Å), O_2 (1.52 Å) and CO_2 (1.16 Å) are similar enough that I assumed that all three gases had the value of K_L calculated using the model in Chapter 3. The difference in pressures inside the lumen and in solution provided the driving force for mass transfer.

The partial pressure of the gas inside the lumen was converted to its equilibrium concentration in the liquid phase using Henry's law. The sodium carbonate solution was assumed to be saturated with air at atmospheric pressure (1 atm). Thus, the concentrations of N_2 and O_2 in solution were also calculated using Henry's law, assuming the solution was saturated with 0.79 atm of N_2 and 0.21 atm of O_2. The molar fluxes for N_2 and O_2 were calculated as follows:

$$\dot{N}_{N_2,\,flux} = K_L(H^{cp}_{N_2}P_{N_2,in} - (0.79\ atm)H^{cp}_{N_2}) \tag{4.9}$$

$$\dot{N}_{O_2,\,flux} = K_L(H^{cp}_{O_2}P_{O_2,in} - (0.21\ atm)H^{cp}_{O_2}) \tag{4.10}$$

The value of K_L used in the model was held constant at 1.31×10^{-3} cm s^{-1}.

In Equations (4.9) and (4.10), if the partial pressure of the inert gases exceeds that of the inert gases in solution, then a positive flux is obtained, indicating that the inert gases diffused out of the membrane lumen. A negative flux indicates diffusion of inert gases into the membrane lumen from the liquid phase.

Relative humidity and the temperature of the effluent gas were measured. To determine the molar flux of water across the membrane, the saturation vapor pressure (P_{sat}) was calculated using the measured temperature values and Antoine's equation with the parameters shown in Table 4.1.

$$P_{sat} = \exp(A - \frac{B}{T+C}) \quad \textbf{(4.11)}$$

Since relative humidity (RH) was measured at the outlet, the partial pressure of effluent water vapor was calculated as follows:

$$P_{H_2O_{out}} = P_{sat} \times \frac{RH}{100} \quad \textbf{(4.12)}$$

The molar flux of water vapor was then calculated using ideal gas law, which utilized the measured effluent volumetric flow rate and temperature. Since the influent gas had no water vapor, the amount of water vapor diffusing across the membrane is equal to the amount of effluent water vapor. The flux of water vapor in the effluent stream was calculated based on the cross-sectional area of the fiber bundle. This flux was then normalized to the mass-transfer area of the membrane using Equation (4.14) to calculate the flux of water vapor across the membrane.

$$\dot{N}_{H_2O_{out}} = \frac{\dot{V}_{out} \times P_{H_2O_{out}}}{R \times T \times A} \quad \textbf{(4.13)}$$

$$\dot{N}_{H_2O_{flux}} = \frac{\dot{N}_{H_2O_{out}} \times A}{SA} \quad \textbf{(4.14)}$$

where SA is the mass-transfer surface area of the membrane calculated using Equation (3.34).

For a closed-end module, neither CO_2 nor H_2O exited the membranes; thus, relative humidity values at the outlet were not measurable. In this case, $\dot{N}_{H_2O_{flux}}$ was calculated using Fick's law. The driving force for H_2O transfer was provided by the difference between the water vapor pressure in the solution (1 atm) and P_{sat}. However, the overall-mass transfer coefficient for the water vapor pressure gradient (K_P, mol m^{-2} Pa^{-1} min^{-1}) was unknown. K_P calculated from experiments with pure CO_2-supplied open-end modules was kept constant for the remainder of the model simulations.

$$K_P = \frac{\dot{N}_{H_2O_{flux}}}{(P_{H_2O_{sat}} - P_{H_2O}} \quad \textbf{(4.15)}$$

The value of K_P was held constant at 3.51×10^{-5} mol m^{-2} Pa^{-1} min^{-1}. $\dot{N}_{H_2O_{flux}}$ for a closed-end HFM was calculated using Equation (4.15) with K_P known, and $P_{H_2O_{sat}}$ calculated using (4.11) and measured gas temperature values.

The effluent molar flux of CO_2 was the difference between the flux across the membrane and the inlet flux.

$$\dot{N}_{CO_2,\,out} = \dot{N}_{CO_2,\,in} - \dot{N}_{CO_2,\,flux} \quad \textbf{(4.16)}$$

Similarly, effluent fluxes for N_2 and O_2 were calculated. The effluent fluxes of each gas in a closed-end HFM was zero since no gas vented out the distal end of the lumen.

The partial pressure of each gas was calculated using equations derived from the ideal gas law, similar to Equations (4.4), (4.5), and (4.6). In this case, the measured outlet volumetric flow rates were used along with the effluent molar flux rates calculated using Equation (4.16). The effluent CO_2 % was calculated and compared with the measured effluent CO_2 %.

$$CO_2\,\% = \frac{P_{CO_2,\,out}}{P_{tot,\,out}} \quad \textbf{(4.17)}$$

With a macroscopic perspective of the HFM module in hand, I investigated the gas concentration profiles inside the fiber lumen. The changes in gas partial pressures and gas fluxes along the fiber length provide insight into the efficacy of membrane mass-transfer area usage. With this information, membrane module construction can be optimized in order to prevent excess usage of fiber bundles, which provides an economic advantage.

The fiber bundle was divided into 50 equal segments such that the change in CO_2 concentration from one segment to the next was extremely small. The length (l_i), cross-sectional area (A), and the surface area (SA_i) of each segment were equal; they were simply the length of one fiber and overall surface area divided by the number of segments (n).

$$l_i = \frac{l}{n} \tag{4.18}$$

$$SA_i = \frac{SA}{n} \tag{4.19}$$

The molar fluxes of the inlet gases were known through measurements and mass balance calculations. The molar fluxes were converted into molar flow rates (mol min^{-1}).

$$\dot{n}_{i,CO_2,in} = \dot{N}_{CO_{2,\,in}} \times A \tag{4.20}$$

$$\dot{n}_{i,N_2,in} = \dot{N}_{N_{2,\,in}} \times A \tag{4.21}$$

$$\dot{n}_{i,N_2,in} = \dot{N}_{N_{2,\,in}} \times A \tag{4.22}$$

The partial pressures of each gas at the inlet of the first segment (P_i) was equal to the partial pressure of each gas in the supply stream. The volumetric flow rate was calculated using ideal gas law with the total pressure (P_i) and total molar flow rate as inputs. The total pressure was used in this case, since the volumetric flow rate calculated from the partial pressure and molar flow rates of each gas was the same as that calculated from the total pressure and total molar flow rate.

$$\dot{V}_{i,tot,in} = \frac{\dot{n}_{i,in} \times R \times T}{P_{i,in}} \tag{4.23}$$

The molar flow rates of each species across the membrane in the segment, in units of mol min^{-1}, were calculated using K_L and the driving force for mass transfer.

$$\dot{n}_{i,CO_2,flux} = K_L(H^{cp}_{CO_2} P_{i,CO_2,in} - [CO_{2,aq}]) \times SA_i \quad \textbf{(4.24)}$$

$$\dot{n}_{i,N_2,flux} = K_L(H^{cp}_{N_2} P_{i,N_2,in} - (0.79\ \text{atm}) H^{cp}_{N_2}) \times SA_i \quad \textbf{(4.25)}$$

$$\dot{n}_{i,O_2,flux} = K_L(H^{cp}_{O_2} P_{i,O_2,in} - (0.21\ \text{atm}) H^{cp}_{O_2}) \times SA_i \quad \textbf{(4.26)}$$

In Equation (4.24), $[CO_{2,aq}]$ was calculated using Equation (3.15). In Equations (4.25) and (4.26), the dissolved concentration of N_2 and O_2 in the bulk phase were calculated using Henry's law, similar to Equations (4.9) and (4.10).

The molar flow rate of water vapor diffusing into one segment of the membrane was calculated using (4.27). The pressure gradient was the difference between the water vapor pressure at the inlet of the segment and the saturation vapor pressure, which provided the driving force to pull water vapor from the bulk solution into the lumen.

$$\dot{n}_{i,H_2O,flux} = K_P(P_{sat} - P_{i,H_2O,in}) \quad \textbf{(4.27)}$$

The total molar flow rate at the end of the segment was calculated using Equation (4.16).

With values for partial pressures, inlet molar and volumetric flow rates, and membrane mass-transfer rates computed, the next step was to calculate the partial pressures and volumetric flow rate at the end of each segment. Pressure and volumetric flow rate are inherently inter-dependent; thus, assumptions need to be made to simplify the calculation. If either pressure or volumetric flow rate is known, then the other variable can be computed.

An open-end system is characterized by gas velocity, resulting in dominant advective transport in the lumen compared with diffusion across the membrane wall. Due to this phenomenon, a pressure drop develops along the fiber length due to frictional losses (Perez-Calleja et al., 2017). Thus, the reasonable assumption for an open-end system would be to fix the volumetric flow rate and gas velocity in the lumen. In contrast, in a closed-end system, the lumen remains pressurized, since gas is not vented out of the distal end. Thus, for closed-end mode, holding constant pressure is the reasonable assumption. Partially open modules are a hybrid combination of open- and closed-end systems. I applied both assumptions separately to partially open systems. My expectation was that the greater the restriction on the effluent flow, the more the module behaves as a closed-end system.

When pressure in the lumen was held constant ($P_{i,in} = P_{i,out}$), then the volumetric flow rate at the end of the segment was calculated by substituting the molar flow rate leaving the segment and $P_{i,in}$ in Equation (4.23). If volumetric flow rate was held constant ($\dot{V}_{i,in} = \dot{V}_{i,out}$), then $P_{i,out}$ was calculated using Equation (4.23).

The partial pressures of each gas leaving the segment was then calculated by substituting the effluent total volumetric flow rate, molar flow rate of each gas, and temperature into Equation (4.23). To compute the velocity of the gas (u_g) leaving the segment, the cross-sectional area was calculated using Equation (4.7). The total volumetric flow rate of the gas leaving the segment was then divided by the cross-sectional area to determine the gas velocity.

$$u_g = \frac{\dot{V}_{i,out,tot}}{A} \quad \textbf{(4.28)}$$

Output values at the exit of a segment serve as input variables at the inlet of the next segment. This calculation is repeated for the number of segments chosen; in this case, 50 segments were chosen.

4.2 Results and Discussion

For modules supplied with pure CO_2, predicted accumulation of inert gases was minimal, as shown in Figure 4.2, which presents the outputs from a module supplied with pure CO_2 under assumptions of constant pressure – Figure 4.2 (a) and (c) – and constant gas velocity – Figure 4.2 (b) and (d). As expected, the assumption of constant pressure described a closed-end system better than the assumption of constant volumetric flow rate. Since gas was not vented out the distal end, the gas velocity at that point was 0, as shown in Figure 4.2 (a). As a result, the lumen remained pressurized with CO_2 due to the supply of pure CO_2. Figure 4.2 (b) shows a pressure drop, which was inaccurate, since pressure was constant in a closed-end HFM. Thus, for the rest of the model calculations, constant pressure was assumed for closed-end systems.

Applying the assumption of constant volumetric flow rate to an open-end system resulted in the model predicting nearly a constant CO_2 partial pressure and total pressure in the fiber lumen, as shown in Figure 4.2 (c). The model predicted the total pressure at the distal end to be 24.39 psia, which was a small decline from the inlet total pressure of

24.55 psia due to loss of CO_2 across the membrane wall. The measured outlet total pressure was 14.08 psia.

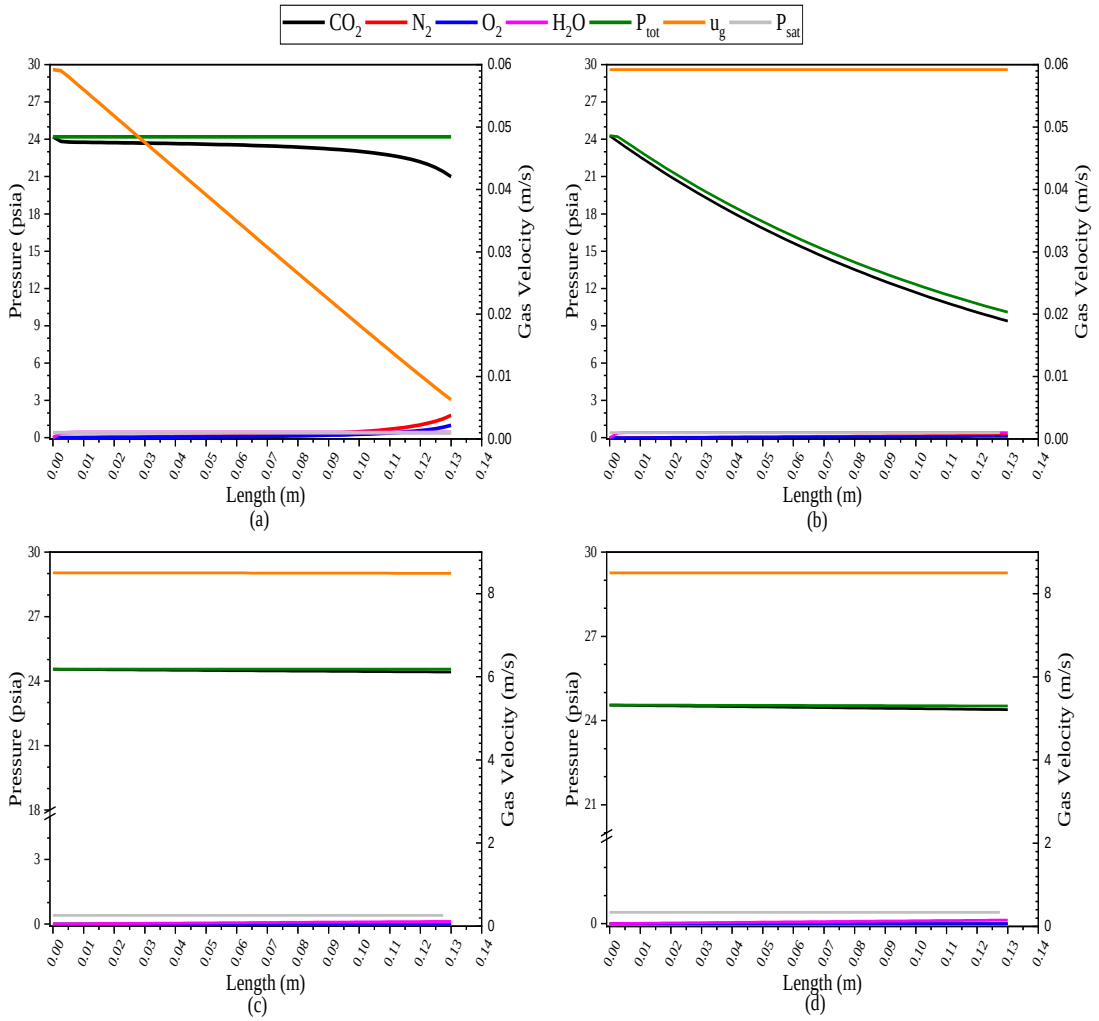

Figure 4.2. Modeled gas concentration profiles for pure CO_2-supplied modules consisting of 32 fibers, 13 cm long under the following conditions: (a) closed-end mode, constant pressure; (b) closed-end mode, constant gas velocity; (c) open-end mode, constant pressure; (d) open-end mode, constant gas velocity.

The large measured loss in total pressure at the outlet in open-end mode could have been caused by frictional losses in the inlet connectors, across the membrane itself, in the outlet connectors, or a combination. Frictional losses were not accounted for in the model, and the pressure drop due solely to frictional losses inside the membrane should not be large (Perez-Calleja et al., 2017). The pressure of the gas could reduce due to the expansion of gas as it flowed from the HFM to the polyurethane tubing. Similarly, the movement of the gas into the HFM from the polyurethane tubing also could have reduce the pressure of the gas due to the presence of a connector at the inlet. However, the pressure drop due to the inlet and outlet connectors was estimated to be <1 psi. It also is possible (and likely) that having the open end exposed to atmospheric pressure caused a large pressure drop. Thus, for the rest of the model calculations, a linear pressure drop between the measured inlet and outlet pressures was imposed for an open-end system, as shown in Figure 4.3.

The gas velocity in the fiber lumen increased in the case shown in Figure 4.3 because of decreasing gas pressure across the lumen. Since pressure and volume are inversely related based on the ideal gas law, a decrease in pressure corresponds to an increase in the volumetric flow rate resulting in an increase in gas velocity. The average gas velocity in an open-end mode in Figure 4.3 was 11 m s^{-1} as compared to 0.033 m s^{-1} in the closed-end mode shown in Figure 4.2 (a).

The accumulation of inert gases was not a significant problem for a module supplied with pure CO_2. Figure 4.2 (a) and Figure 4.3 show that the partial pressure of

inert gases in the lumen was low. For a closed-end system, the partial pressure of CO_2 remained high throughout the membrane, decreasing only slightly towards the distal end. Since the driving force for CO_2 transfer was very high due to its high solubility relative to N_2 and O_2, the back-diffusion of inert gases was low. At the distal end, the model predicted N_2 and O_2 partial pressures of 1.80 and 0.99 psia, respectively. For an open-end system, the model predicted N_2 and O_2 partial pressures of approximately 0 psia; thus, the CO_2 partial pressure was approximately equal to the total gas pressure, as shown in Figure 4.3.

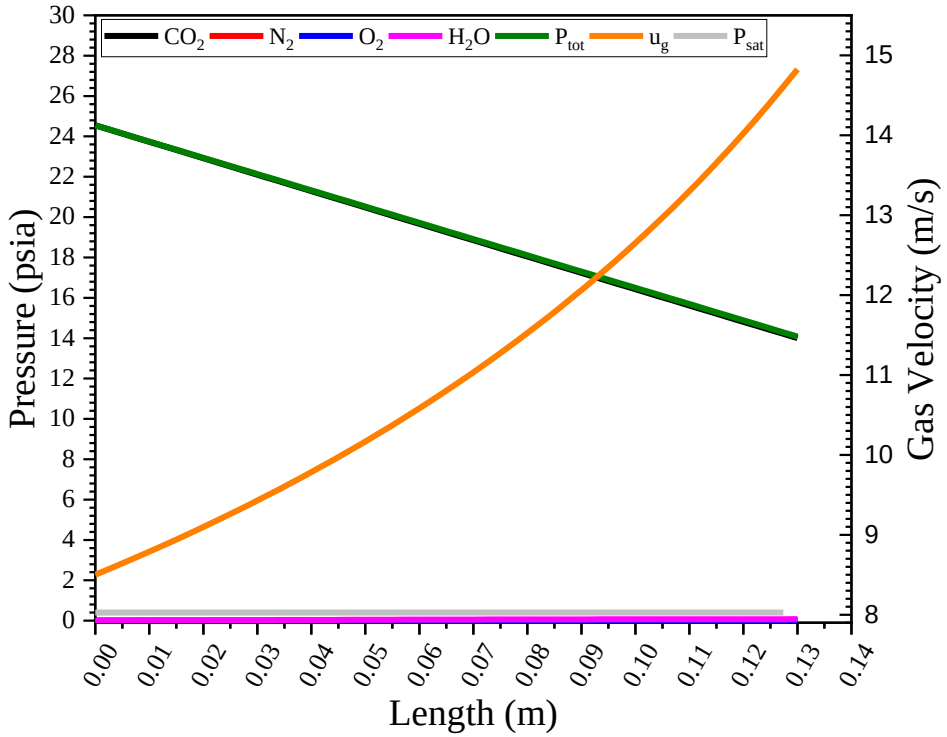

Figure 4.3. Modeled gas concentration profiles for a pure CO_2-supplied module consisting of 32 fibers, 13 cm long operated in open-end mode.

Figure 4.4 shows the fluxes of CO_2, N_2, O_2, and H_2O for a module supplied with pure CO_2. The CO_2 flux was much higher than the fluxes of inert gases due to the high CO_2 partial pressure in the lumen. CO_2 decreased towards the distal end of a closed-end HFM due to accumulation of inert gases, which kept the lumen pressurized at constant pressure, while the CO_2 flux decreased in the open-end system due to the pressure drop. H_2O flux was high in the proximal end of the lumen due to the large transmembrane concentration gradient, but decreased rapidly as the vapor pressure in the lumen approached saturation vapor pressure, thus diminishing the driving force. In contrast, in the open-end mode, the H_2O flux did not decrease rapidly due to a low vapor pressure in the lumen, which kept the driving force for H_2O transfer relatively high. CO_2 flux decreased along the fiber lumen with a decrease in CO_2 partial pressure, mainly due to a drop in the total gas pressure across the lumen. The overall flux for the closed-end module and open-end module was the same at approximately 2900 g m^{-2} day^{-1}. The K_La value also was the same for both modules, 0.26 hr^{-1}. This suggests that, for pure CO_2, the influence of inert gases in open-end and closed-end HFMs was negligible.

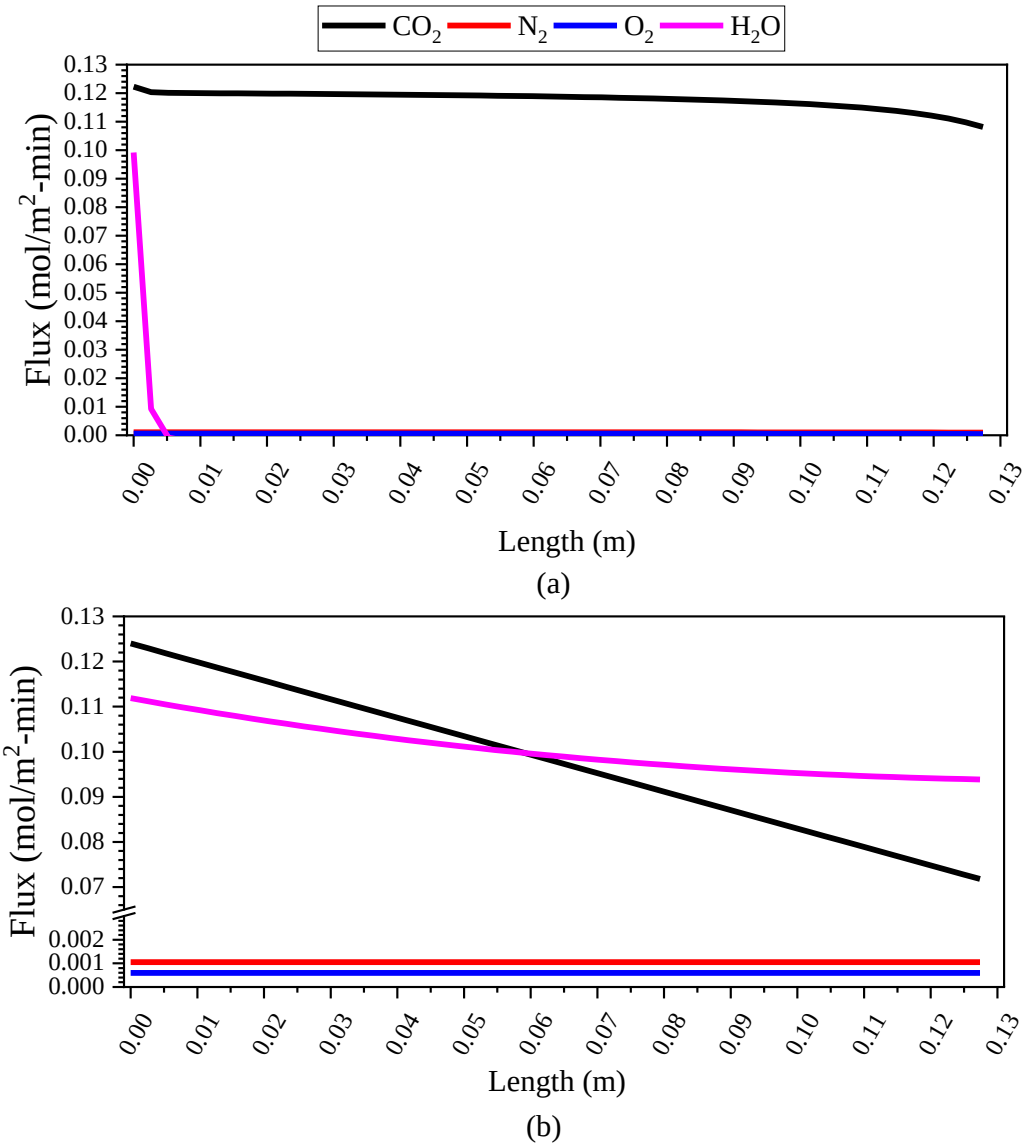

Figure 4.4. Modeled fluxes for a 32-fiber module, using 13-cm long fibers supplied with pure CO_2 and operated in (a) closed-end mode and (b) open-end mode.

As the concentration of inert gases in the supply stream increased, the accumulation of inert gases at the distal end of the lumen became significant, as shown in Figure 4.5. The intra-membrane gas velocity was far lower in closed-end mode than an

open-end mode, because the inlet volumetric flow rate into a closed-end HFM was much lower than that for an open-end HFM due to the lack of effluent flow. In both cases, the gas velocity was lower than HFMs supplied with pure CO_2. The maximum available membrane mass-transfer area was not utilized for CO_2 transfer, as the CO_2 partial pressure dropped to 0 at a fiber length of 4.5 cm, as shown in Figure 4.5 (a). Thus, only 26% of the fiber length was used for CO_2 transfer. Based on an effective fiber length of 4.5 cm, the effective specific mass-transfer area used was calculated to be 1.81 m^{-1}, which was 26% of the maximum a value for a 32-fiber bundle, 17-cm long, which was 6.84 m^{-1}. The flux and K_La values derived from the model in Section 3.3 were 574 g m^{-2} day^{-1} and 0.074 hr^{-1} respectively, for the closed-end HFM. Based on the K_La value calculated using the pH-based model and the maximum K_L value of 1.31×10^{-3} cm s^{-1}, an effective area of 0.56 m^{-1} was calculated. This corresponds to an effective fiber length of 1.4 cm. This value is much lower than the model-predicted value of 4.5 cm obtained here. The overestimation of model-predicted values may be due to inaccurate measurements of inlet volumetric flow rates by the flow meters at low flow rates.

With a high average gas velocity of 10 m s^{-1} in the open-end HFM, the CO_2 partial pressure decreased as the total gas pressure approached atmospheric pressure at the distal end of the lumen. The partial pressure of inert gases was higher than that for the pure CO_2-supplied open-end module shown in Figure 4.4, due to the higher concentration in the supply gas stream. The flux and K_La value estimated from the model in Section 3.3 for this HFM were 2630 g m^{-2} day^{-1} and 0.342 hr^{-1}. The K_La value, in this case, was higher than for the closed-end HFM, as well as for the value obtained for pure

CO_2-supplied HFMs, indicating that the mass-transfer area was more efficiently utilized for CO_2 uptake.

The model-predicted outlet partial pressures of 12.6, 1.11, 0.30, and 0.08 psia for CO_2, N_2, O_2, and H_2O, respectively, compared well with values 12.1, 1.07, 0.28, and 0.11 psia estimated via the entire-system mass balance. The conclusion here is that the model accurately represented all partial pressures.

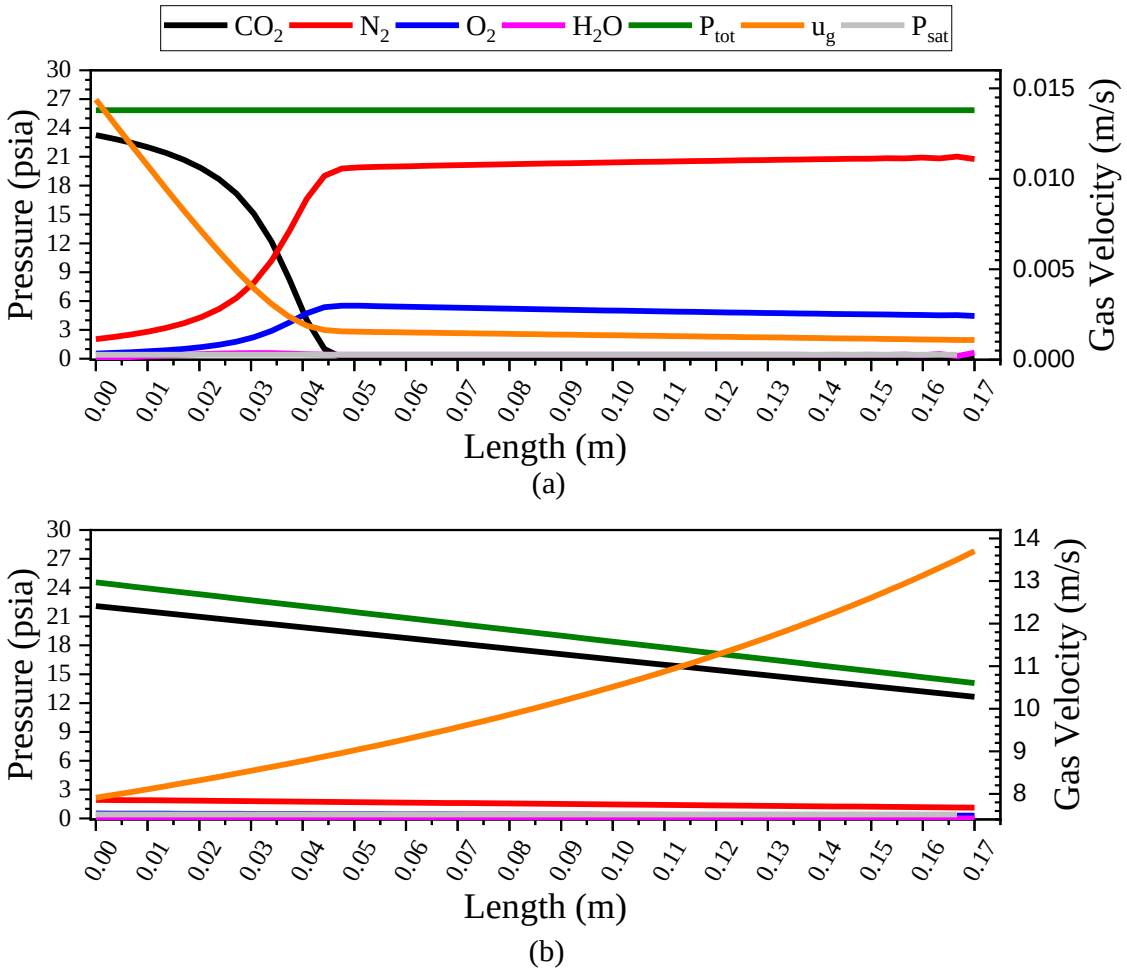

Figure 4.5. Modeled gas concentration profiles for 90% CO_2-supplied modules consisting of 32 fibers, 17-cm long under the following conditions: (a) closed-end mode and (b) open-end mode.

Figure 4.6 (a) shows that the CO_2 flux decreased in a closed-end system as the partial pressure decreased, while, in an open-end system, the flux remained constant along with the partial pressure. The fluxes of inert gases were negligible compared to CO_2 flux.

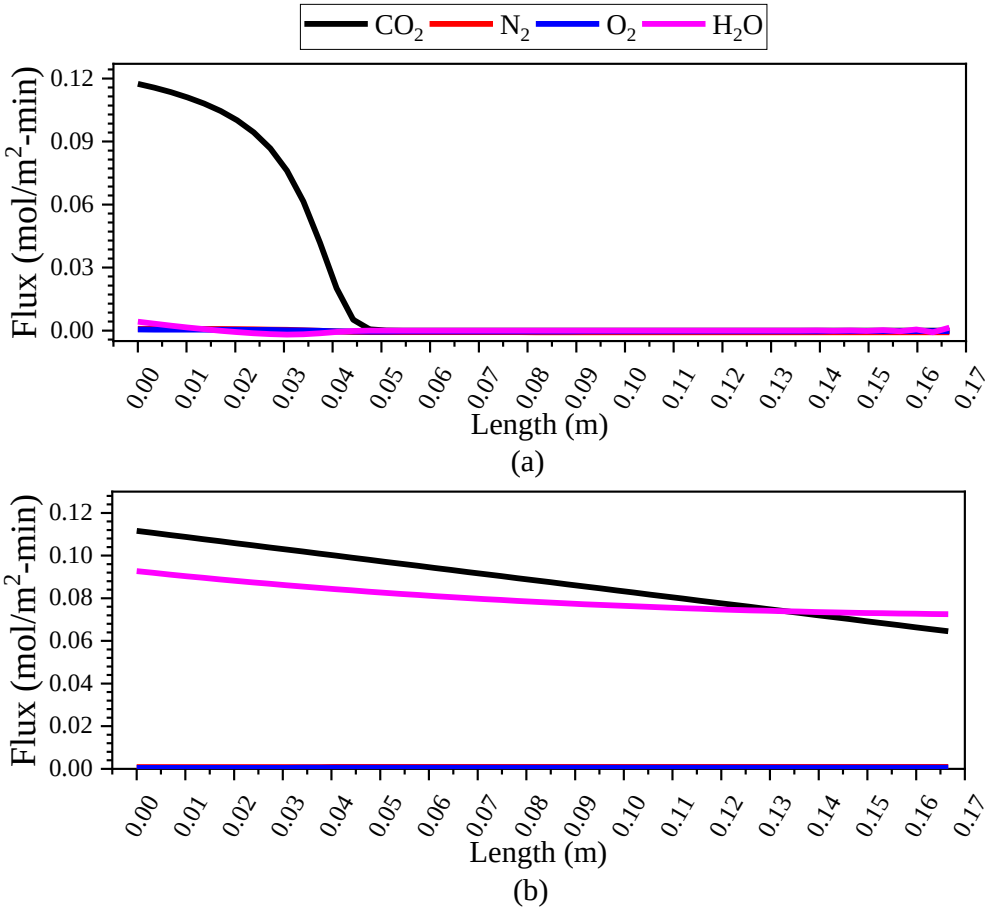

Figure 4.6. Modeled flux profiles for 90% CO_2-supplied modules consisting of 32 fibers, 17-cm long under the following conditions: (a) closed-end mode and (b) open-end mode.

Figure 4.7 shows the gas profiles for a module supplied with 10% CO_2. The partial pressure of CO_2 did not drop to 0 in closed-end mode. The high partial pressure of inert gases, particularly N_2, reduced the flux of CO_2 across the membrane enough that partial pressure could not be driven to 0. Similar to the previous case, the CO_2 partial pressure in open-end mode was nearly constant; however, its magnitude was far lower

due to the dilute concentration of CO_2 in the supply gas stream. Since CO_2 was present throughout the membrane, CO_2 diffusion into the bulk liquid phase occurred all along the fiber length, as shown in Figure 4.8. The flux and K_La estimated from the model in Section 3.3 for the closed-end HFM were 38 g m^{-2} day^{-1} and 0.044 hr^{-1} respectively; the open-end HFM had a flux of 183 g m^{-2} day^{-1} and a K_La of 0.213. Thus, the effective a was 0.34 m^{-1} for the closed-end HFM, and 1.63 m^{-1} for the open-end HFM. The maximum a for this module was 6.84 m^{-1}.

For the open-end HFM, the model predicted an effluent CO_2 partial pressure of 1.51 psia, compared with 1.47 psia estimated from the mass balance. The model estimated partial pressures for N_2, O_2 and H_2O at 10.8, 2.87 and 0.10 psia respectively, comparing well with 10.4, 2.77 and 0.10 psia estimated by the mass balance.

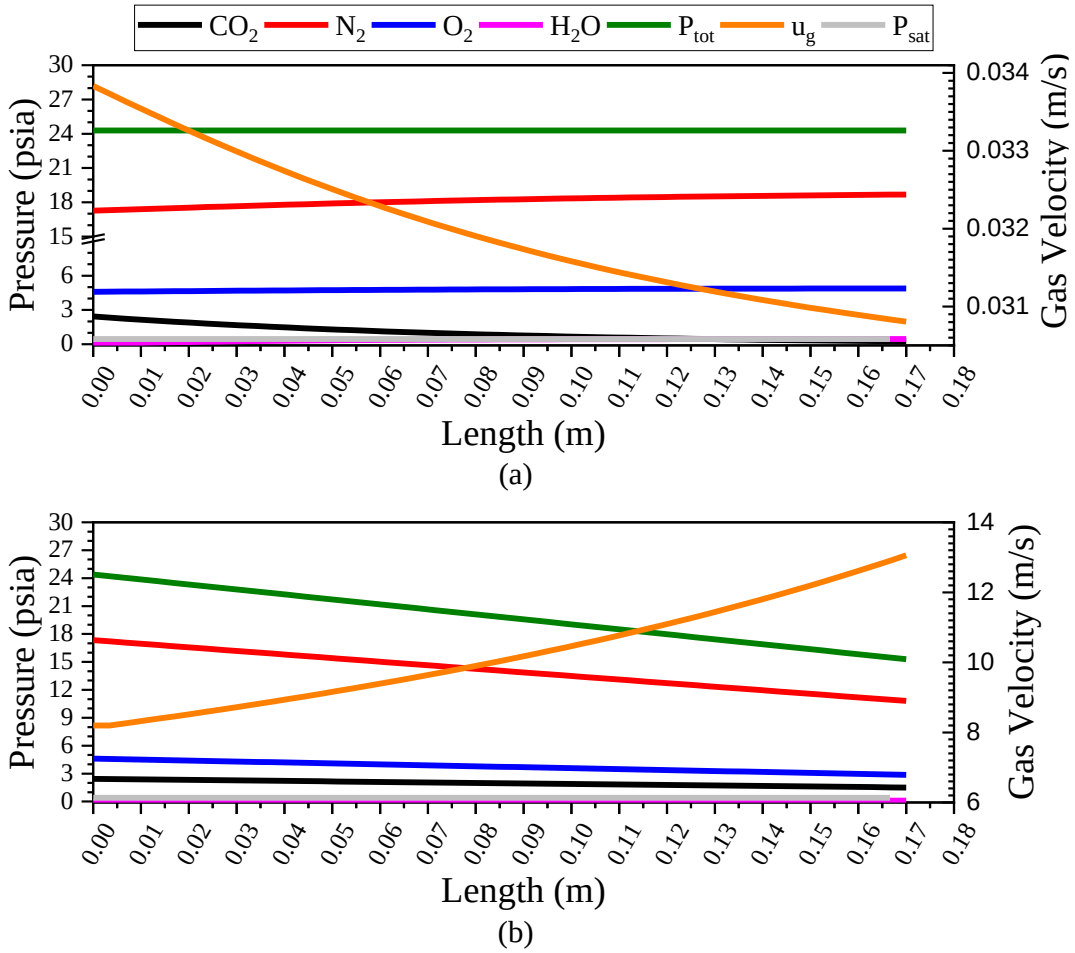

Figure 4.7. Modeled gas concentration profiles for 10% CO_2-supplied modules consisting of 32 fibers, 17-cm long under the following conditions: (a) closed-end mode and (b) open-end mode.

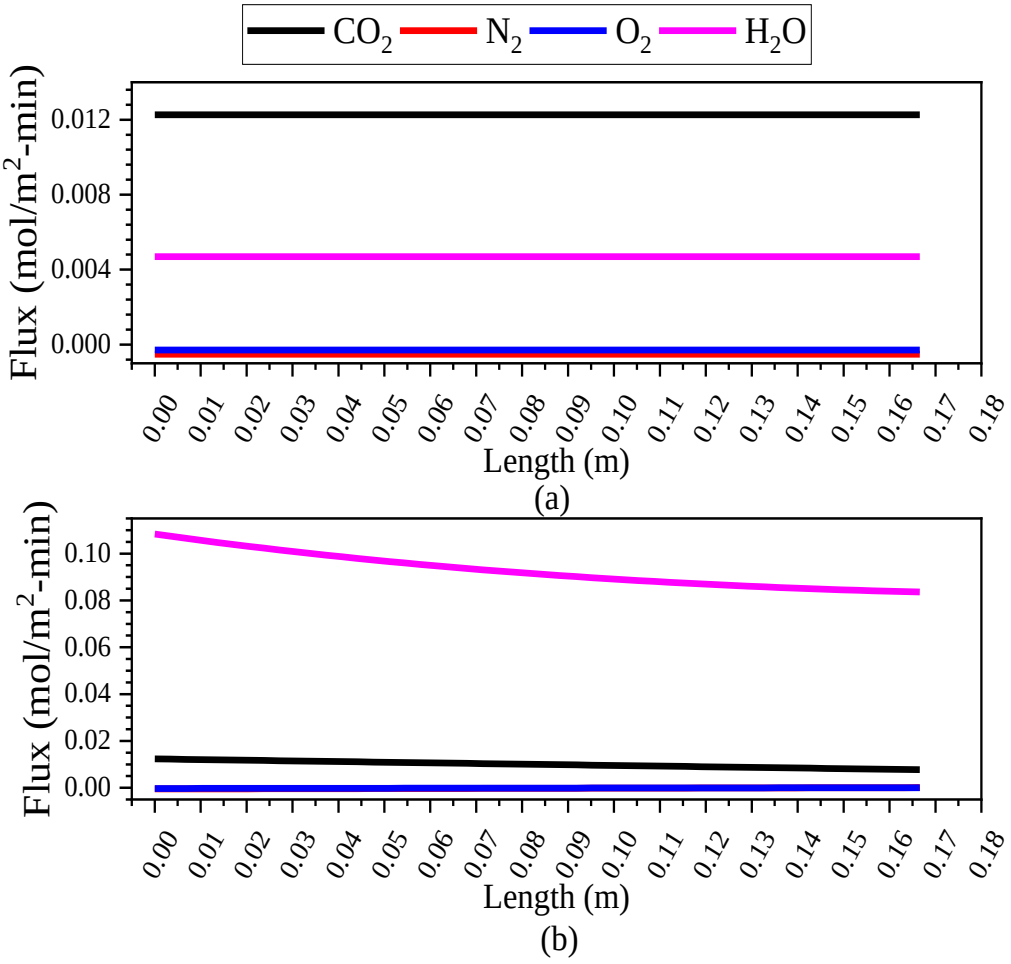

Figure 4.8. Modeled flux profiles for 10% CO_2-supplied modules consisting of 32 fibers, 17-cm long under the following conditions: (a) closed-end mode and (b) open-end mode.

Figure 4.9 shows the gas profiles for a partially open-ended HFM. The degree to which the effluent volumetric flow rate was restricted dictates whether the system showed characteristics of a closed-end system or open-end system. The restricted effluent flow rate was calculated based on the flow rate through the lumen if the module was operated in open-ended mode. For this module, the open-ended flow rate was

approximately 400 ccm; in Figure 4.9 (a) and (c), the effluent flow rate was restricted to roughly 1% of this value, or 3.7 ccm. Similarly, in the other two cases, the flow rate was restricted to 10% and 50% of the open-ended value.

CO_2 flux decreased as the effluent flow rate was decreased. For the 1% case, the flux was 299 g m^{-2} day^{-1}, while the flux was 340 and 365 g m^{-2} day^{-1} for the 10% and 50% cases respectively. The K_La values followed a similar trend, but were not vastly different either, with values 0.041, 0.047 and 0.050 hr^{-1} for the 1%, 10%, and 50% cases, respectively. The gas velocity in the lumen was highest for the 50% case. Based on this and the similar gas profile, the 50% case behaved almost like an open-end system, while the 1% case behaved almost like a closed-end system.

The model-predicted outlet pressure was 24.2 psia and 15.5 psia for Figure 4.9 (a) and (b), respectively, compared with the measured value of 24.2 psia. This suggests that the assumption of constant pressure applied better to a system with a highly restricted effluent flow, and it reinforces that the 1% cases behaves similarly to a closed-end HFM. A similar conclusion was reached for the 10% case, since the model-predicted outlet pressure values for Figure 4.9 (c) and (d) were 23.5 psia and 21.2 psia, respectively, compared with a measured value of 23.5 psia. For the 50% case, the model-predicted value for Figure 4.9 (e) and (f) was 24.0 psia for both assumptions; the measured value was 20.7 psia. This suggests that the pressure drop due to gas expansion at the outlet increased as the distal end became more open and the volumetric flow rate increased.

The effluent CO_2 % calculated by the model was 11.9% and 18.5% for Figure 4.9 (a) and (b), respectively, 43.2% and 43.5% for Figure 4.9 (c) and (d), respectively, and 49.2% and 49.9% for Figure 4.9 (e) and (f), respectively. Thus, a relationship between the effluent flow rate and the amount of CO_2 exiting the system was clear.

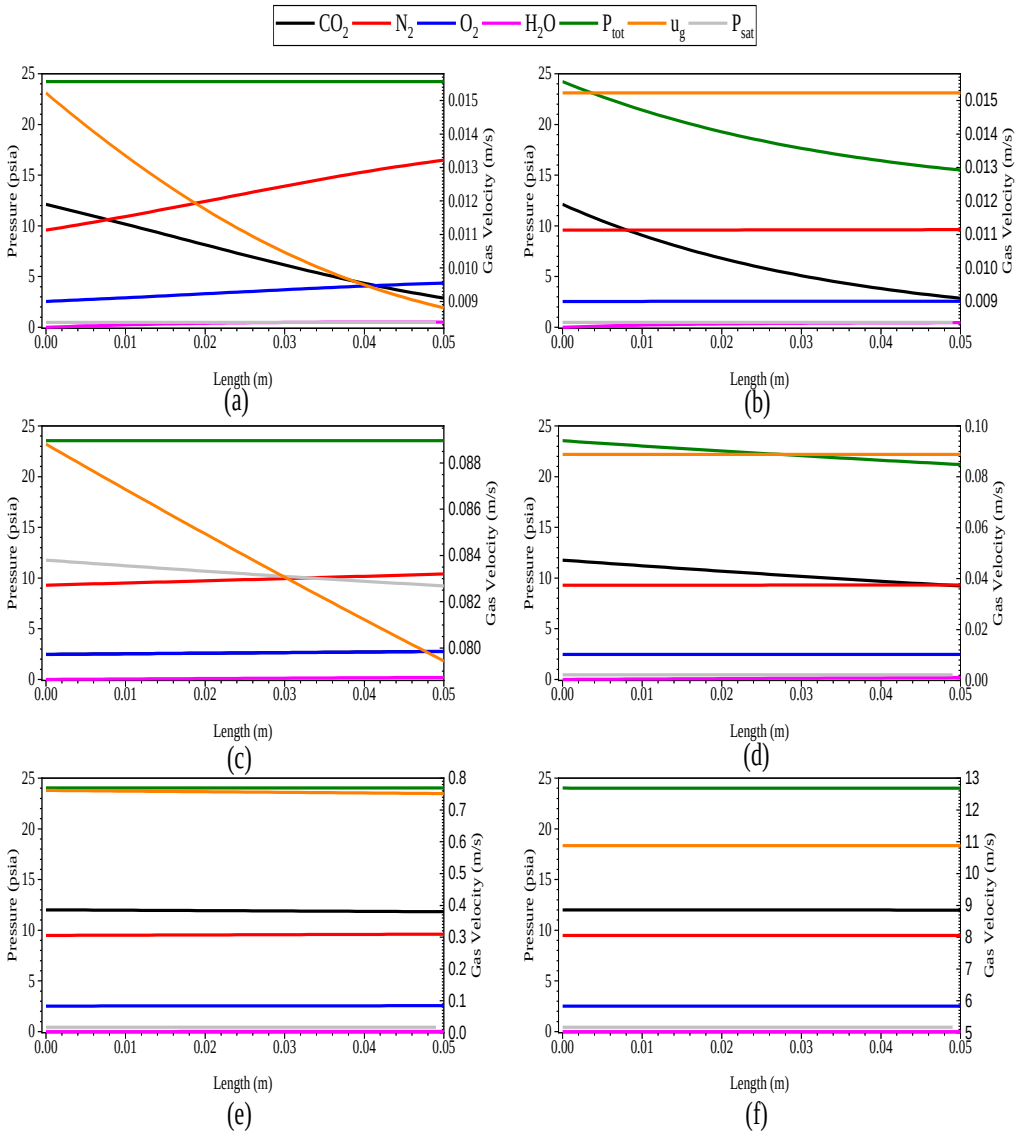

Figure 4.9. Modeled gas concentration profiles for partially open-ended, 64-fiber module 5-cm long supplied with 50% CO_2 for effluent flow rates of: (a) 3.7 ccm, constant pressure; (b) 3.7 ccm, constant gas velocity; (c) 38 ccm, constant pressure; (d) 38 ccm, constant gas velocity; (e) 210 ccm, constant pressure; and (f) 210 ccm, constant gas velocity.

As shown in Table 4.2, the CO_2-transfer efficiency for modules supplied pure-CO_2 and operated with an open-end was poor compared with partially open systems. The transfer efficiency depicted here is the ratio of the amount of CO_2 transferred across the membrane, calculated as the difference between the amount of CO_2 in the influent and effluent stream, to the amount of CO_2 in the input stream. In an open-ended module, a large percentage of CO_2 supplied was vented out, resulting in poor transfer efficiencies: The CO_2 % efficiency was as low as 0.27%, and the highest value with pure CO_2 was only 0.33%. Clearly, operating with a fully open end is not realistic due to the near total loss of CO_2 from venting.

Also shown in Table 4.2 is that a closed-end HFM was 100% efficient at transferring CO_2 across the membrane, but much of the fiber was not active in CO_2 delivery due to the buildup of inert gases when the inlet gas was not pure CO_2 (Figures 4.5 and 4.7). Thus, the kinetics of CO_2 delivery were slowed significantly by the accumulation of inert gases when the input of $\leq$ 90% CO_2.

Partially open-end modules that restricted the effluent flow rate to 1% of its open-end mode value regained high transfer efficiency: up to 88% (Table 4.2). This improvement was possible because of low gas velocity through the lumen still swept some of the accumulated inert gases out through the distal end, but without incurring a large loss of CO_2.

Table 4.2. Modeled fluxes and transfer efficiencies for HFMs.

CO_2 Content (%)	Operating Condition	No. of Fibers	Fiber Length (m)	Flux ($g\ m^{-2}\ day^{-1}$)	CO_2 Transfer Efficiency (%)
100	Closed	32	0.13	2879	100
100	Open	32	0.13	2929	0.27
100	Closed	32	0.17	2622	100
100	Open	32	0.17	3195	0.32
100	Closed	32	0.18	2545	100
100	Open	32	0.18	2626	0.33
90	Closed	32	0.17	574	100
90	Open	32	0.17	2638	0.36
90	Partially open, 1%	64	0.37	539	88
90	Partially open, 10%	64	0.37	731	40
90	Partially open, 50%	64	0.37	557	10
90	Partially open, 1%	64	0.39	421	63
90	Partially-open, 10%	64	0.39	413	30
90	Partially-open, 50%	64	0.39	746	15

Table 4.3 shows that increasing fiber length in a module increased the transfer efficiency at higher volumetric flow rates. While the transfer efficiency remained highest for modules with a restricted effluent flow rate of 1%, the transfer efficiency increased significantly for higher effluent flow rates in longer-fiber HFMs. It is possible that, for longer fibers, the residence time of the gas in the lumen was higher than for shorter fibers. Additionally, the accumulation of inert gases may have become significant as fiber length increased, resulting in the disadvantage of lower CO_2 flux for longer fibers.

Table 4.3. Modeled fluxes and transfer efficiencies evaluated for partially open-ended HFMs supplied with 50% CO_2.

Operating Condition	No. of Fibers	Fiber Length (m)	Flux ($g\ m^{-2}\ day^{-1}$)	CO_2 Transfer Efficiency (%)
Partially open, 1%	64	0.05	299	11
Partially open, 10%	64	0.05	340	2.5
Partially open, 50%	64	0.05	365	0.27
Partially open, 1%	64	0.10	306	20
Partially open, 10%	64	0.10	360	3.8
Partially open, 50%	64	0.10	408	1.0
Partially-open, 1%	64	0.39	68	78
Partially-open, 10%	64	0.39	253	29
Partially-open, 50%	64	0.39	236	6.8

The rate-limiting step for CO_2 delivery was the diffusion of CO_2 through the liquid-phase boundary layer into the bulk liquid phase. In some cases, the slow transfer of CO_2 gas from the membrane wall to the bulk liquid phase led to the formation and attachment of CO_2 bubbles at the external membrane surface. This is illustrated in Figure 4.10 for delivery of pure CO_2. A possible cause for bubble formation was the low mixing intensity, which resulted in a large external diffusion layer and slow diffusion kinetics. Increasing mixing or reducing CO_2 partial gas pressures should eliminate or reduce

bubble formation on the external surface of the HFM. Bubble formation is undesired because it opens up the possibility for loss of CO_2 gas to the atmosphere, instead of transfer to the liquid to form DIC.

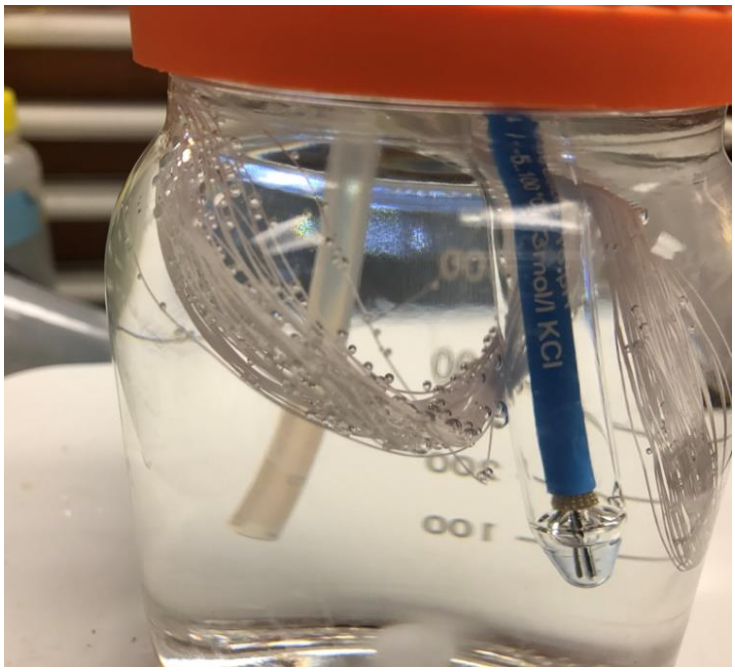

Figure 4.10. Bubble formation observed on the external surface of a closed-end HFM receiving pure CO_2.

Table 4.4 shows the CO_2 transfer efficiencies for the sparging system evaluated. The sparging system performed better than the open-end systems, but worse than the partially open-end and closed HFMs. The transfer efficiencies shown could be over-estimated, since the amount of CO_2 off-gassed was not measured for the sparging system.

Table 4.4. Modeled fluxes and transfer efficiencies evaluated for the sparging system

Inlet CO_2 Content (%)	CO_2 Transfer Efficiency (%)
100	36
90	45
50	37
10	34

CHAPTER 5

CONCLUSION AND FUTURE WORK

5.1 Conclusion

In this thesis, I first developed a model to estimate mass-transfer coefficients and CO_2-transfer rates across the MC membrane based on the experimentally measured rate of change in pH. The model accurately calculated transfer rates between a pH range of 10 – 8. The validity of the model was established by comparing predicted DIC concentrations with measured values. The method used by the DIC instrument in this project required acidification of samples, resulting in the measured DIC values being lower than predicted values due to CO_2 off-gassing. Additionally, the rate of CO_2 off-gassing was found to increase at pH < 8. Since the model did not account for CO_2 off-gassing, the model was accurate only within a pH range of 10 – 8, where the rate of CO_2 off-gassing (or in-gassing) was minimal.

While K_La values predicted by the model were accurate, the values of K_L estimated were not constant for each case when using the geometric area of the HFM that for a. This means that the effective surface area of the membranes was not constant, but decreased as CO_2 depleted inside the HFM. A maximum K_L value of 1.31×10^{-3} cm s^{-1} was obtained from modules tested with pure CO_2, in which CO_2 depletion was minimal.

Using a kinetic mass-balance model for gas transfer processes in and out of the membrane lumen, I investigated the performances of closed-end and open-end HFM modules for transferring CO_2. The advantage of a closed-end module is 100% CO_2 transfer efficiency, since no gas exits the distal end of the lumen. Open-end modules are characterized by high transfer rates. For modules supplied pure CO_2, closed-end HFMs performed better than open-end HFMs, because a closed-end HFM remained pressurized with CO_2, maintaining a high CO_2 partial pressure in the lumen. In open-end mode, a pressure drop developed across the fiber due to high gas velocity resulting in frictional losses in the lumen. Additionally, the expansion of gas at the outlet as it passed from the fiber lumen into the connection tubing led to a decline in total pressure. A CO_2 flux as high as 3400 g m^{-2} day^{-1} was obtained for a closed-end HFM, compared with 2400 g m^{-2} day^{-1} for an identical open-end HFM supplied with pure CO_2. The K_La values obtained for both modes were similar at ~ 0.3 hr^{-1}.

As the CO_2 concentration in the supply stream was reduced, open-end HFMs performed significantly better than closed-end HFMs, since the accumulation of inert gases became a significant factor affecting CO_2 transfer. A CO_2 flux of 750 g m^{-2} day^{-1} was obtained for the HFM mentioned above when operated in closed-end mode and supplied with 90% CO_2. The CO_2 flux increased to 2150 g m^{-2} day^{-1} when the mode of operation was switched to open-end. The flux was observed to decrease as the concentration of CO_2 supplied decreased from 90% to 10% of the influent gas. The K_La also followed the same trend as the flux, decreasing as the mode of operation was switched from closed-end to open-end, and as the inlet CO_2 concentration was reduced.

For CO_2-enriched air, open-end HFMs performed better than closed-end HFMs by maintaining a higher CO_2 partial pressure in the lumen by venting accumulated inert gases. However, transfer efficiencies for open-end HFMs were < 1% because of high gas throughput. The transfer efficiencies for closed-end HFM were 100%, except when the formation of bubbles on the external membrane surface prevented mass balance closure. Bubbles formed because the rate-limiting step was the diffusion of bubbles from the gas phase to the bulk liquid phase at the exterior surface of the HFM.

Operating HFMs in a partially open-end mode offered advantages over closed-end and open-end modes when the CO_2 supply was less than 100% CO_2. HFMs operated with a 1% gas throughput (compared to open-end operation) had transfer efficiencies of up to 88%, while mitigating declines in flux. Longer fibers operated in partially open-end mode appeared to have higher transfer efficiencies and lower transfer rates than shorter fibers supplied with CO_2-enriched air.

5.2 Future work

The model developed in Chapter 3 to estimate mass-transfer coefficients and CO_2 fluxes can be improved in order to predict more accurate K_L values. K_L in the model was computed based on the CO_2 partial pressure and flux across the membrane. Since the CO_2 partial pressure is not necessarily constant throughout the fiber, the average partial pressure is lower than that in the supply stream. Thus, an iterative model could be

developed in order to calculate K_L and the CO_2 partial pressure in the lumen based on CO_2 flux and the known maximum K_L value computed for pure CO_2-supplied modules.

This model was also developed under the assumption of ideality and low ionic activity in solution. For a complex culture growth medium, the model could potentially overestimate CO_2 flux values, since the various ionic interactions in solution would not be accounted for. The Debye-Huckel equation could be used to provide reasonable estimates for the activity coefficients which affect the equilibrium constants. These new equilibrium constants could then be utilized in the model to provide realistic flux and mass-transfer coefficient values.

Operating HFMs in partially open-end mode and restricting the effluent flow rate to 1% appeared to have the best performance in terms of providing both high transfer efficiencies and reasonable transfer rates. Increasing the length of the fiber decreased the transfer rates while simultaneously increasing transfer efficiencies. Further experiments should be conducted to test HFM performance based on the number of fibers and the fiber length. This would provide useful information in optimizing module design for large-scale systems. Furthermore, periodic venting of gases is a novel approach to combine the benefits of closed-end and open-end mode. HFMs operating in closed-end mode could be switched to open-end mode of operation briefly at regular time intervals in order to prevent inert gas accumulation and maintain a uniform CO_2 profile in the fiber lumen.

The model developed in Chapter 4 does not predict the pressure drop in an open-end HFM. The gas could experience a pressure drop due to reduction and expansion as it enters and exits the fiber lumen, respectively. Factoring this phenomenon along with frictional losses could help provide an accurate pressure profile as a function of the fiber length. Additionally, the model required the assumption of either constant pressure or constant volumetric flow rate in the fiber. Differential equations could be developed and calculated using numerical methods in order to facilitate the simultaneous estimation of pressure, volumetric flow rate and fluxes in the fiber lumen.

REFERENCES

Ahmed T, Semmens MJ. 1992a. Use of sealed end hollow fibers for bubbleless membrane aeration - Experimental studies. *J. Memb. Sci.* **69**:1–10.

Ahmed T, Semmens MJ. 1992b. The use of independently sealed microporous hollow fiber membranes for oxygenation of water - Model development. *J. Memb. Sci.* **69**:11–20.

Ahmed T, Semmens MJ, Voss MA. 2004. Oxygen transfer characteristics of hollow-fiber, composite membranes. *Adv. Environ. Res.* **8**:637–646.

American Physical Society. 2011. Direct Air Capture of CO2 with Chemicals.

Barnwal BK, Sharma MP. 2005. Prospects of biodiesel production from vegetables oils in India. *Renew. Sustain. Energy Rev.* **9**:363–378.

Baz-Rodríguez S, Aguilar-Corona A, Soria A. 2012. Rising velocity for single bubbles in pure liquids. *Rev. Mex. Ing. Química* **11**:269–278. http://www.redalyc.org/articulo.oa?id=62026895006.

Becker EW. 1994. Microalgae: Biotechnology and microbiology. Camrbidge: Cambridge University Press.

Bhola V, Swalaha F, Ranjith Kumar R, Singh M, Bux F. 2014. Overview of the potential of microalgae for CO2 sequestration. *Int. J. Environ. Sci. Technol.*

Bilanovic D, Andargatchew A, Kroeger T, Shelef G. 2009. Freshwater and marine microalgae sequestering of CO2 at different C and N concentrations - Response surface methodology analysis. *Energy Convers. Manag.* **50**:262–267.

Blanken W, Schaap S, Theobald S, Rinzema A, Wijffels RH, Janssen M. 2017. Optimizing carbon dioxide utilization for microalgae biofilm cultivation. *Biotechnol. Bioeng.* **114**:769–776. http://doi.wiley.com/10.1002/bit.26199.

BP Energy Outlook. 2018. BP Energy Outlook. https://www.bp.com/content/dam/bp/en/corporate/pdf/energy-economics/energy-outlook/bp-energy-outlook-2018-global-insights.pdf.

Brennan L, Owende P. 2010. Biofuels from microalgae—A review of technologies for production, processing, and extractions of biofuels and co-products. *Renew. Sustain. Energy Rev.* **14**:557–577. https://www.sciencedirect.com/science/article/pii/S1364032109002408.

Campbell PK, Beer T, Batten D. 2009. Greenhouse gas sequestration by algae-

Energy and greenhouse gas life cycle studies.

Carvalho AP, Malcata FX. 2000. Effect of culture media on production of polyunsaturated fatty acids by Pavlova lutheri. *Cryptogam. Algol.* **21**:59–71.

Carvalho AP, Malcata FX. 2001. Transfer of carbon dioxide within cultures of microalgae: Plain bubbling versus hollow-fiber modules. *Biotechnol. Prog.* **17**:265–272.

Carvalho AP, Meireles LA, Malcata FX. 2006. Microalgal Reactors: A Review of Enclosed System Designs and Performances. *Biotechnol. Prog.* **22**:1490–1506.

Chisti Y. 2008. Biodiesel from microalgae beats bioethanol. *Trends Biotechnol.* **26**:126–131.

Crutzen PJ, Mosier AR, Smith KA, Winiwarter W. 2008. N2O release from agro-biofuel production negates global warming reduction by replacing fossil fuels. *Atmos. Chem. Phys.* **8**:389–395.

Davis R, Aden A, Pienkos PT. 2011. Techno-economic analysis of autotrophic microalgae for fuel production. *Appl. Energy* **88**:3524–3531.

Eustance E, T. Wray J, Badvipour S, R. Sommerfeld M. 2016. Volatile Nutrients - Improving Utilization of Ammonia and Carbon Dioxide in Microalgal Cultivation: A Review. *Curr. Biotechnol.* **5**:130–141. http://www.eurekaselect.com/openurl/content.php?genre=article&issn=2211-5501&volume=5&issue=2&spage=130.

Fan LH, Zhang YT, Cheng LH, Zhang L, Tang DS, Chen HL. 2007. Optimization of carbon dioxide fixation by Chlorelia vulgaris cultivated in a membrane-photobioreactor. *Chem. Eng. Technol.* **30**:1094–1099.

Fan LH, Zhang YT, Zhang L, Chen HL. 2008. Evaluation of a membrane-sparged helical tubular photobioreactor for carbon dioxide biofixation by Chlorella vulgaris. *J. Memb. Sci.* **325**:336–345.

Ferreira BS, Fernandes HL, Reis A, Mateus M. 1998. Microporous hollow fibres for carbon dioxide absorption: Mass transfer model fitting and the supplying of carbon dioxide to microalgal cultures. *J. Chem. Technol. Biotechnol.* **71**:61–70.

Goldman JC, Azov Y, Riley CB, Dennett MR. 1982. The effect of pH in intensive microalgal cultures. I. Biomass regulation. *J. Exp. Mar. Bio. Ecol.* **57**:1–13. https://www-sciencedirect-com.ezproxy1.lib.asu.edu/science/article/pii/002209818290140X.

Hill GA. 2006. Measurement of Overall Volumetric Mass Transfer Coefficients for Carbon Dioxide in a Well-Mixed Reactor Using a pH Probe. *Ind. Eng. Chem. Res.*

45:5796–5800. https://pubs.acs.org/doi/abs/10.1021/ie060242t.

Johnson DW, Semmens MJ, Gulliver JS. 1997. Diffusive transport across unconfined hollow fiber membranes. *J. Memb. Sci.* **128**:67–81. https://www-sciencedirect-com.ezproxy1.lib.asu.edu/science/article/pii/S0376738896003237.

Kadam KL. 1997. Power plant flue gas as a source of CO 2 for microalgae cultivation: Economic impact of different process options. *Energy Convers. Manag.* **38**:S505–S510.

Keith DW. 2009. Why Capture CO2 from the Atmosphere? *Science (80-.).* **325**:1654–1655.

Keith DW, Holmes G, St. Angelo D, Heidel K. 2018. A Process for Capturing CO 2 from the Atmosphere. *Joule* **0**. http://linkinghub.elsevier.com/retrieve/pii/S2542435118302253.

Kendall A, Chang B. 2009. Estimating life cycle greenhouse gas emissions from corn-ethanol: a critical review of current US practices. *J. Clean. Prod.* **17**:1175–1182.

Kim G, Choi W, Lee C-H, Lee K. 2013. Enhancement of dissolved inorganic carbon and carbon fixation by green alga Scenedesmus sp. in the presence of alkanolamine CO2 absorbents. *Biochem. Eng. J.* **78**:18–23. https://www-sciencedirect-com.ezproxy1.lib.asu.edu/science/article/pii/S1369703X13000491.

Kim HW, Marcus AK, Shin JH, Rittmann BE. 2011. Advanced Control for Photoautotrophic Growth and CO2-Utilization Efficiency Using a Membrane Carbonation Photobioreactor (MCPBR). *Environ. Sci. Technol.* **45**:5032–5038.

Klausner A. 1986. Algaculture - Food for thought. *Bio-Technology* **4**:947-.

Kreulen H, Smolders CA, Versteeg GF, Vanswaaij WPM. 1993. Microporous hollow-fiber membrane modules as gas-liquid contactors. 1. Physical mass-transfer processes - A specific application - Mass-transfer in highly viscous liquids. *J. Memb. Sci.* **78**:197–216.

Kulkarni MG, Dalai AK. 2006. Waste cooking oil-an economical source for biodiesel: A review. *Ind. Eng. Chem. Res.* **45**:2901–2913.

Kumar A, Ergas S, Yuan X, Sahu A, Zhang Q, Dewulf J, Malcata FX, van Langenhove H. 2010. Enhanced CO2 fixation and biofuel production via microalgae: recent developments and future directions. *Trends Biotechnol.*

Lackner K, Grimes P, Ziock H-J. 2001. Capturing carbon dioxide from air. *... Carbon Sequestration* 1-15 p. https://www.netl.doe.gov/publications/proceedings/01/carbon_seq/7b1.pdf.

Lackner KS. 2009. Capture of carbon dioxide from ambient air. *Eur. Phys. J. Spec. Top.*

Lackner KS. 2013. The thermodynamics of direct air capture of carbon dioxide. *Energy* **50**:38–46.

Lackner KS. 2003. A guide to CO2 sequestration. *Science (80-.).*

Lee YK, Hing HK. 1989. Supplying CO2 to photosynthetic algal cultures by diffusion through gas-permeable membranes. *Appl. Microbiol. Biotechnol.* **31**:298–301.

Lewis NS, Nocera DG. 2007. Powering the planet: Chemical challenges in solar energy utilization. *Proc. Natl. Acad. Sci. U. S. A.* **104**:20142.

Li Y, Horsman M, Wu N, Lan CQ, Dubois-Calero N. 2008. Biofuels from microalgae. *Biotechnol. Prog.* **24**:815–820.

Lower SK. 1999. Carbonate equilibria in natural waters. *Chem1 Virtual Textb.* Simon Fraser University, Burnaby, British Columbia, Canada. http://www.chem1.com/acad/webtext/pdf/c3carb.pdf.

Manganaro JL, Lawal A, Goodall B. 2015. Techno-economics of microalgae production and conversion to refinery-ready oil with co-product credits. *Biofuels Bioprod. Biorefining-Biofpr* **9**:760–777.

Miron AS, Garciia MCC, Gomez AC, Camacho FG, Grima EM, Chisti Y. 2003. Shear stress tolerance and biochemical characterization of Phaeodactylum tricornutum in quasi steady-state continuous culture in outdoor photobioreactors. *Biochem. Eng. J.* **16**:287–297.

Moore A. 2008. Biofuels are dead: long live biofuels(?) - Part one. *N. Biotechnol.* **25**:6–12.

Naik SN, Goud V V., Rout PK, Dalai AK. 2010. Production of first and second generation biofuels: A comprehensive review. *Renew. Sustain. Energy Rev.* **14**:578–597. https://www.sciencedirect.com/science/article/pii/S1364032109002342.

Nakićenović N, Intergovernmental Panel on Climate Change. Working III G. 2000. Special report on emissions scenarios : a special report of Working Group III of the Intergovernmental Panel on Climate Change. *Emiss. Scenar.* Cambridge: Cambridge : Cambridge University Press.

Nguyen BT, Rittmann BE. 2015. Predicting Dissolved Inorganic Carbon in Photoautotrophic Microalgae Culture via the Nitrogen Source. *Environ. Sci. Technol.* **49**:9826–9831. https://doi.org/10.1021/acs.est.5b01727.

Nguyen BT, Rittmann BE. 2016. Effects of inorganic carbon and pH on growth kinetics of Synechocystis sp. PCC 6803 ☆. https://ac-els-cdn-com.ezproxy1.lib.asu.edu/S2211926416300832/1-s2.0-S2211926416300832-main.pdf?_tid=a360083e-6b0a-4a7d-9174-4d4753b7af09&acdnat=1523499700_8d032b52c32d78226d9019e33b27267a.

Nielsen ES, Jensen PK. 1958. Concentration of carbon dioxide and rate of photosynthesis in Chlorella pyrenoidosa. *Physiol. Plant.* **11**:170–180.

Ono E, Cuello JL. 2006. Feasibility Assessment of Microalgal Carbon Dioxide Sequestration Technology with Photobioreactor and Solar Collector. *Feasibility Assess. Microalgal Carbon Dioxide Sequestration Technol. with Photobioreactor Sol. Collect.* **95**:597–606.

Perez-Calleja P, Aybar M, Picioreanu C, Esteban-Garcia AL, Martin KJ, Nerenberg R. 2017. Periodic venting of MABR lumen allows high removal rates and high gas-transfer efficiencies. *Water Res.* **121**:349–360.

Pielke R, Wigley T, Green C. 2008. Dangerous assumptions. *Nature* **452**:531–532.

Price GD. 2011. Inorganic carbon transporters of the cyanobacterial CO2 concentrating mechanism. *Photosynth. Res.* **109**:47–57. http://link.springer.com/10.1007/s11120-010-9608-y.

Putt R, Singh M, Chinnasamy S, Das KC. 2011. An efficient system for carbonation of high-rate algae pond water to enhance CO2 mass transfer. *Bioresour. Technol.* **102**:3240–3245.

Quinn JC, Davis R. 2015. The potentials and challenges of algae based biofuels: A review of the techno-economic, life cycle, and resource assessment modeling. *Bioresour. Technol.*

Rahaman MSA, Cheng LH, Xu XH, Zhang L, Chen HL. 2011. A review of carbon dioxide capture and utilization by membrane integrated microalgal cultivation processes. *Renew. Sustain. Energy Rev.* **15**:4002–4012. http://dx.doi.org/10.1016/j.rser.2011.07.031.

Raupach MR, Marland G, Ciais P, Le Quere C, Canadell JG, Klepper G, Field CB. 2007. Global and regional drivers of accelerating CO2 emissions. *Proc. Natl. Acad. Sci. U. S. A.* **104**:10288–10293.

Sadeghizadeh A, Farhad Dad F, Moghaddasi L, Rahimi R. 2017. CO2 capture from air by Chlorella vulgaris microalgae in an airlift photobioreactor. *Bioresour. Technol.* **243**:441–447.

Sander R. 2015. Compilation of Henry's law constants (version 4.0) for water as

solvent. *Atmos. Chem. Phys* **15**:4399–4981. www.atmos-chem-phys.net/15/4399/2015/.

Sawayama S, Inoue S, Dote Y, Yokoyama SY. 1995. CO2 fixation and oil production through microalga. *Energy Convers. Manag.* **36**:729–731.

Schenk PM, Thomas-Hall SR, Stephens E, Marx UC, Mussgnug JH, Posten C, Kruse O, Hankamer B. 2008. Second Generation Biofuels: High-Efficiency Microalgae for Biodiesel Production. *BioEnergy Res.* **1**:20–43. http://link.springer.com/10.1007/s12155-008-9008-8.

Sims REH, Mabee W, Saddler JN, Taylor M. 2010. An overview of second generation biofuel technologies. *Bioresour. Technol.* **101**:1570–1580. https://www.sciencedirect.com/science/article/pii/S0960852409015508?via%3Dihub.

Smith JM, van Ness HC, Abbott MM. 2005. Introduction to chemical engineering thermodynamics. Ed. H C (Hendrick C.) Van Ness, Michael M Abbott. *Chem. Eng. Thermodyn.* 7th ed.. New York: New York : McGraw-Hill.

Solomon S, Plattner GK, Knutti R, Friedlingstein P. 2009. Irreversible climate change due to carbon dioxide emissions. *Proc. Natl. Acad. Sci. U. S. A.* **106**:1704–1709.

Stumm W, Morgan JJ. 1996. Aquatic chemistry: chemical equilibria and rates in natural waters. Ed. James J Morgan 3rd ed..

Sun A, Davis R, Starbuck M, Ben-Amotz A, Pate R, Pienkos PT. 2011. Comparative cost analysis of algal oil production for biofuels. *Energy* **36**:5169–5179.

Talbot P, Gortares MP, Lencki RW, de la Noüe J. 1991. Absorption of CO_2 in algal mass culture systems: A different characterization approach. *Biotechnol. Bioeng.* **37**:834–842. http://www.ncbi.nlm.nih.gov/pubmed/18600683.

Tang Y, Zhou C, Van Ginkel SW, Ontiveros-Valencia A, Shin J, Rittmann BE. 2012. Hydrogen permeability of the hollow fibers used in H2-based membrane biofilm reactors. *J. Memb. Sci.* **407**–**408**:176–183. https://www.sciencedirect.com/science/article/pii/S0376738812002311.

Tapie P, Bernard A. 1988. Microalgae production - Technical and economic evaluations. *Biotechnol. Bioeng.* **32**:873–885.

Tebbani S, Rayen F, Lopes F, Dumur D, Dominique P. 2014. CO2 Biofixation by Microalgae : Automation Process. Wiley-ISTE.

Terry KL, Raymond LP. 1985. System-design for the autotrophic production of microalgae. *Enzyme Microb. Technol.* **7**:474–487.

U.S. Energy Information Administration. 2005. International Energy Outlook 2005. Washington, DC: U.S. Department of Energy. https://www.eia.gov/outlooks/archive/ieo05/pdf/0484(2005).pdf.

U.S. Energy Information Adminstration. 2017. International Energy Outlook 2017 Overview. *Int. Energy Outlook.* Vol. IEO2017 143 p. https://www.eia.gov/outlooks/ieo/pdf/0484(2017).pdf%0Awww.eia.gov/outlooks/ieo.

Ugwu CU, Aoyagi H, Uchiyama H. 2008. Photobioreactors for mass cultivation of algae. *Bioresour. Technol.* **99**:4021–4028.

Voss MA, Ahmed T, Semmens MJ. 1999. Long-term performance of parallel-flow, bubbleless, hollow-fiber-membrane aerators. *Water Environ. Res.* **71**:23–30.

Wang B, Li YQ, Wu N, Lan CQ. 2008. CO2 bio-mitigation using microalgae. *Appl. Microbiol. Biotechnol.* **79**:707–718.

Wang M, Lawal A, Stephenson P, Sidders J, Ramshaw C. 2011a. Post-combustion CO2 capture with chemical absorption: A state-of-the-art review. *Chem. Eng. Res. Des.* **89**:1609–1624.

Wang T, Lackner KS, Wright A. 2011b. Moisture swing sorbent for carbon dioxide capture from ambient air. *Environ. Sci. Technol.*

Wijffels RH, Barbosa MJ. 2010. An outlook on microalgal biofuels. *Science* **329**:796.

World Energy Council. 2017. World Energy Trilemma Index 2017: Monitoring the sustainability of national energy systems. https://www.worldenergy.org/wp-content/uploads/2017/11/Energy-Trilemma-Index-2017-Report.pdf.

Xu H, Miao XL, Wu QY. 2006. High quality biodiesel production from a microalga Chlorella protothecoides by heterotrophic growth in fermenters. *J. Biotechnol.* **126**:499–507.

Yen HW, Ho SH, Chen CY, Chang JS. 2015. CO2, NOx and SOx removal from flue gas via microalgae cultivation: A critical review. *Biotechnol. J.* **10**:829–839.

Yun YS, Lee SB, Park JM, Lee CI, Yang JW. 1997. Carbon dioxide fixation by algal cultivation using wastewater nutrients. *J. Chem. Technol. Biotechnol.* **69**:451–455.

Zheng Q, Martin GJO, Kentish SE. 2016. Energy efficient transfer of carbon dioxide from flue gases to microalgal systems. *Energy Environ. Sci.* **9**:1074–1082. http://dx.doi.org/10.1039/C5EE02005K.

Zhu LD. 2015. Microalgal culture strategies for biofuel production: a review. *Biofuels Bioprod. Biorefining-Biofpr* **9**:801–814.